Lifetimes of the ^{21}Ne 2796-, 1747-, and 2867-keV levels

E. K. Warburton, J. W. Olness, and C. J. Lister
Brookhaven National Laboratory, Upton, New York 11973
(Received 3 November 1978; revised manuscript received 26 April 1979)

The mean lives of the ^{21}Ne $1/2^+$, $7/2^+$, and $9/2^+$ levels at 2796, 1747, and 2867 keV have been measured using the ^{4}He(^{18}O,n)^{21}Ne reaction near threshold and the Doppler shift attenuation method. The results were 7.9 ± 1.0, 74 ± 6, and 61 ± 6 fs, respectively. In order to obtain a result for the 8-fs 2796-keV level, four different targets were used. These consisted of ^{4}He implanted in thick backings of Mg, Al, Ta, and Au. The analysis developed for measuring this fast lifetime is described in detail. Excitation energies of 1747.2 ± 0.3, 2788.87 ± 0.10, 2795.8 ± 0.7, and 2867.2 ± 0.4 keV were obtained for the second-to-fifth excited states. The lifetime results are compared to recent shell-model predictions.

[NUCLEAR REACTIONS ^{4}He(^{18}O,n)^{21}Ne, $E = 20$–27 MeV; measured Doppler-shift attenuation and lineshape. ^{21}Ne 2796-, 1747-, and 2867-keV levels; deduced τ_m. Implanted targets.]

I. INTRODUCTION

It has recently[1,2] been pointed out that the $J^\pi = \frac{1}{2}^-, \frac{1}{2}^+$ doublet in ^{21}Ne at 2789 and 2796 keV provides a very favorable possibility for the study of the parity nonconserving weak interaction in the nucleus.

Such parity mixing would result in a nonzero circular polarization (P_γ) for the 2789-keV ground-state decay (see Fig. 1), and a recent measurement[3] put an upper limit of 0.5% on P_γ. An alternative method to investigate such mixing would be to measure the asymmetry (A_γ) of the 2789-keV ground-state decay following formation of this level using a polarized beam. To obtain the parity mixing matrix element from either P_γ or A_γ, a constant of proportionality[4] must be evaluated which requires knowledge of $\tau(M1)$, the partial mean life of the $M1$ part of the $\frac{1}{2}^+ \rightarrow \frac{3}{2}^+$ 2796 → 0 transition. The 2796-keV level decays predominantly to the ground state, and as the $E2$ contribution is negligible,[4] the measurement of the total mean life of this level allows an evaluation of this constant which is necessary for present and future parity nonconserving experiments in ^{21}Ne.

An accurate measurement of this lifetime is discussed in this paper. The 2796-keV level was known to have a mean life of $\tau < 20$ fs[5-7] so that an evaluation of the required accuracy involved using the Doppler shift attenuation (DSA) method at the limit of its applicability and also the development of new facets of this technique. Thus a detailed description of the experimental method and analysis of data has been given with emphasis on the many factors which must be taken into consideration in such a measurement. The precision obtained is competitive with the most accurate previous results in the 1–10 fs lifetime range.

The lifetimes of the 1747- and 2867-keV levels (see Fig. 1) also reported herein are considerably longer[5,6,8-11] than that of the 2796-keV level and could thus be extracted using well established γ-ray line shape fitting techniques.[12-14] However, they are also sufficiently short-lived to be analyzed by the technique developed for the 2796-keV level, and permit a convenient comparison between the two methods.

The stopping power of ions in matter provides the most important ancillary input to any DSA measurement. In the next section we present the data and formalism used for the stopping of ^{21}Ne ions in matter and then describe the DSA methods applicable in the present analysis. Some further details of the stopping power are discussed in an Appendix. In Sec. III the experimental results and their analysis are described. Finally, the methods used and the results obtained are compared to previous work in Sec. IV and matrix elements extracted from the experimental lifetimes are compared to shell-model predictions.

II. THE DSA ANALYSIS

A. The specific energy loss of ^{21}Ne and its parametrization

The DSA measurements for the ^{21}Ne 2796-keV level were performed at a ^{21}Ne recoil velocity of $\beta(\equiv v/c) \simeq 0.04$. Thus, accurate results for the energy loss are desired near this velocity and, to a lesser extent, at lower velocities. We consider the specific energy loss $dE/d(\rho x)$ of an ion with nuclear charge Z_1, mass A_1, and velocity v, in a material with nuclear charge Z_2, mass A_2, and density ρ. $dE/d(\rho x)$ is composed of a nuclear part, only important at low velocities ($v/v_0 \lesssim 1$,

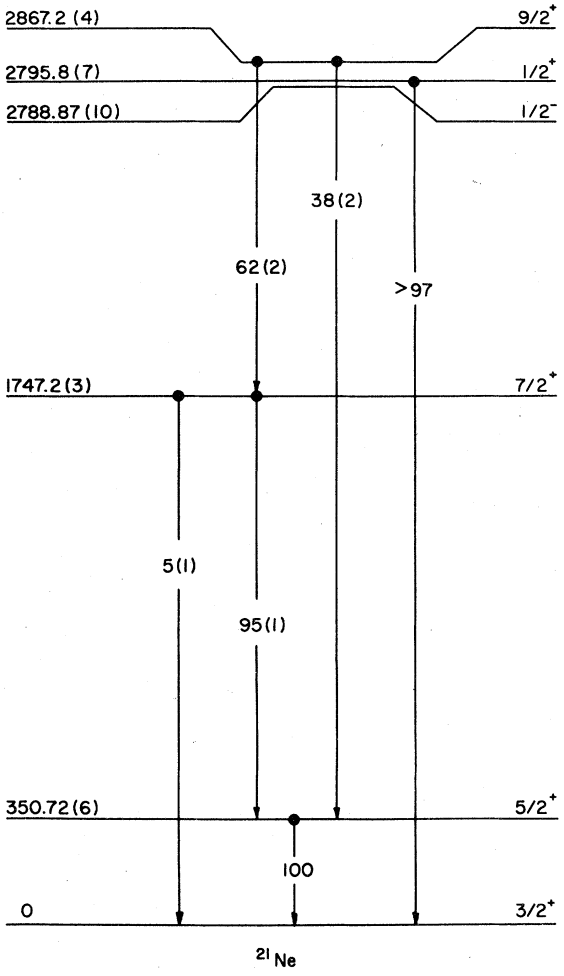

FIG. 1. The ^{21}Ne energy levels for $E_x < 3.6$ MeV and the γ-ray transitions pertinent to the present study. The level energies (in keV) are from the present study except for the first (Ref. 5) and the fifth—which is based on the energy of the 2.87 → 1.75 transition (Ref. 5) and the present excitation energy of the 1.75-MeV level. The spin-parity assignments and branching ratios are from Ref. 5. The numbers in parentheses are the uncertainties in the least significant figure.

where $v_0 = c/137$), and an electronic part. The specific energy loss of ^{21}Ne ions was obtained from a mixture of empirical and semi-empirical results. Porat and Ramavataram[15] provided accurate (±5%) electronic energy loss data for Ne ions stopping in Al, Ni, and Au for the velocity range $0.9 \leq v/v_0 \leq 3.52$. For Ne projectiles, this data provided the main input for Northcliffe and Schilling's encyclopedic tabulation[16] of semi-empirical stopping powers. For Al, further data in the range $6.4 < v/v_0 < 20$ was provided by Northcliffe.[17] For Ne in Al the tabulation of Northcliffe and Schilling is quite reliable since, in their semi-empirical fits, stopping powers for various ions in Al provided the master reference curves for interpolation to other projectiles and materials. Because the experimental results of Porat and Ramavataram provided direct input, the stopping-power curves of Northcliffe and Schilling for Ne ions in Ni and Au are also relatively reliable. In recent years increasingly detailed and accurate stopping power data have revealed departures from the smooth dependence of $dE/d(\rho x)$ on Z_1 and Z_2 assumed by Northcliffe and Schilling. There exist several quite successful effective charge prescriptions for taking these oscillations into account in the interpolation procedures necessary to obtain stopping-power curves where no experimental data exist. We have considered four of these in order to obtain the best results for Ne ions in Mg and Ta—for which no direct measurements exist—and to check the interpolation of Northcliffe and Schilling for Ne in Ni and Au. All four procedures rely on the assumption that for two ions a and b at the same velocity in the same stopping material, the stopping powers are related by

$$\frac{1}{(\gamma Z_1)_b^2}\left(\frac{dE}{d(\rho x)}\right)_b = \frac{1}{(\gamma Z_1)_a^2}\left(\frac{dE}{d(\rho x)}\right)_a , \tag{1}$$

where γ, the effective charge parameter, is assumed to depend on v and Z_1 only. The four procedures used are as follows:

(*i*) *Ward.* Ward *et al.*[18] constructed a careful parametrization of effective charge good for $v/v_0 \geq 2$. Following their prescription, the desired stopping-power curve for a given ion may be obtained from an accurate table of ^{4}He stopping-power data for that material, using their effective charge parametrization and the relationship given by Eq. (1). We have followed this procedure to construct a computer program based on the ^{4}He tables of Ziegler and Chu.[19]

(*ii*) *Forster.* Forster *et al.*[20] made measurements for $Z_1 = 9$, 12, 13, 16, and 17 stopping in elements with $Z_2 = 22$, 26, 28, 29, 47, and 79. They then used the effective charge parametrization of (i) to interpolate to other values of Z_1 for the above values of Z_2.

(*iii*) *Schwalm.* Schwalm *et al.*[21] developed an approach utilizing measurements of $dE/d(\rho x)$ for protons and an associated analytical representation of the effective charge. The Schwalm parametrization is especially adapted to $10 \leq Z_1 \leq 17$ and $11 \leq Z_2 \leq 17$.

(*iv*) *Braune.* Braune[22] combined the effective charge parametrization of (i) with an analytic representation of a "universal materials" function [$F(Z_2; \Xi(V))$ in Eq. (22) of Ref. 21] which quite successfully reproduces the Z_2 oscillations described, e.g., in Ref. 18.

The predictions of (i)–(iv), and of Northcliffe

TABLE I. Comparison of various effective charge prescriptions for $-dE/d(\rho x)$ for ^{21}Ne ions at $v/v_0 = 5.5$.

Stopping material	Energy loss (MeV cm^2/mg) Forster[a]	Ward[b]	Schwalm[c]	Braune[d]	Northcliffe[e]	Average[f]
Mg	...	10.67	9.74	10.11	...	10.17(4.6)
Al	...	9.26	8.93	9.43	9.58	9.30(3.0)
Ni	6.56	6.96	6.67	6.95	6.62	6.75(2.8)
Ta	...	3.50	3.49	3.48	3.50	3.49(0.3)
Au	3.62	3.62	3.34	3.31	3.31	3.44(4.8)

[a] Reference 20.
[b] Reference 18.
[c] Reference 21.
[d] Reference 22.
[e] Reference 16.
[f] The numbers in parentheses give the internal errors in percent.

and Schilling for Ne ions of velocity $v/v_0 = 5.5$ ($\beta \simeq 0.04$) in five materials are compared in Table I. The results are in remarkably good agreement—the averages all have internal errors of <5%. For lower velocities, however, the five $dE/d(\rho x)$ curves constructed for each stopping material are not in such good agreement. Upon consideration of the various curves it was decided that a representation as good as any is that of Northcliffe and Schilling which, after all, is most directly related to the data of Porat and Ramavataram.[15] Accordingly, the values of $dE/d(\rho x)$ used for stopping in Al, Ni, Ta, and Au were the curves of Northcliffe and Schilling scaled to pass through the average values of Table I at $v/v_0 = 5.5$. For stopping in Mg, the ratio of $dE/d(\rho x)$ for ^{20}Ne in Mg and Al, as obtained by the predictions of Schwalm *et al.*,[21] was used to interpolate the results of Northcliffe and Schilling from $Z_2 = 13$ to $Z_2 = 12$.

The above approach gives the electronic energy loss only. Following procedures developed previously at this laboratory[13,23-25] we parametrize the total specific energy loss as

$$-M\frac{dv_z}{dt} \equiv \frac{-dE}{d(\rho x)} = K_n(v/v_0)^{-1} + K_e(v/v_0) - K_3(v/v_0)^3 \qquad (2a)$$

for $0 \leq v \leq v_c$ and

$$-M\frac{dv_z}{dt} \equiv \frac{-dE}{d(\rho x)} = A + B(v/v_0) - C(v/v_0)^2 \qquad (2b)$$

for $v > v_c$, where the initial direction of the recoiling ion is taken as the z axis. Following previous considerations for similar kinematical conditions,[21] we chose K_n equal to 1.26 times the Bohr estimate[26] of the nuclear energy loss evaluated at $v/v_0 = 1$. It should be kept in mind that $K_n(v/v_0)^{-1}$, which represents the nuclear stopping power, is intended to simulate the change with time of both the magnitude *and direction* of v. Thus, throughout the remainder of this paper it is understood that v and v_z are interchangeable. The parameters v_c/v_0, K_e, K_3, A, B, and C were varied to obtain the best fit to the data just described with the constraint that both $-dE/d(\rho x)$ and its derivative were continuous at $v = v_c$. Data for $v/v_0 < 1.9$ were excluded from the fit because this region is not important for present purposes and because the presence of Z_1 oscillations at low velocities render the interpolation procedures relatively unreliable in this velocity region. The results of the least squares fits are displayed in Table II. With the exception of v_c/v_0 (dimensionless), the constants of Eq. (2) appearing in Table II are all in units of MeV cm^2/mg.

A quantity more directly applicable to the DSA than $dE/d(\rho x)$ is $d(v/v_0)/dt$ which we term the slowing power. We obtain [see Eq. (2)]

$$\frac{d(v/v_0)}{dt}(\mathrm{ps}^{-1}) = 4.4105(\rho/A_1)\frac{dE}{d(\rho x)}\left[\frac{\mathrm{MeV\,cm^2}}{\mathrm{mg}}\right], \qquad (3)$$

with ρ in g/cm^3 and A_1 in u. In Fig. 2 curves of $d(v/v_0)/dt$ for ^{21}Ne in Mg, Al, Ta, and Au are shown for the $dE/d(\rho x)$ of Table II. Also shown in Fig. 2 is the relationship between flight time and v/v_0 for an initial velocity $v_i/v_0 = 5.5$. The four stopping materials of Fig. 2 constitute a convenient set which encompasses a wide range of slowing powers. For example, at $v/v_0 = 5.5$ the slowing powers are in the ratio Mg:Al:Ta:Au = 1:1.42:3.34:3.82 ps^{-1}.

B. Application of the DSA to fast lifetimes

We wish to develop a simple formalism useful in understanding the application of the DSA to very fast lifetimes and applicable to the present measurement of the 2796-keV level. The concepts are quite similar to a previous treatment of Branford

TABLE II. Parameters for the energy loss of Ne ions in five materials. The parametrization is given in the text.

Stopping material	K_n [a]	K_e	K_3	v_c/v_0	A	B	C	ϵ (%) [b]	Range of v/v_0 [c]
Mg	0.378	3.310	0.050	4.940	11.006	0.126	0.051	0.8	1.9–9.0
Al	0.354	3.113	0.051	4.534	8.118	0.639	0.078	0.7	1.9–9.0
Ni	0.287	1.766	0.000	2.300	−1.181	2.956	0.271	0.9	1.9–6.3
Ta	0.141	0.801	0.000	3.000	−1.131	1.601	0.136	1.6	2.0–6.3
Au	0.134	0.781	0.000	3.000	−1.072	1.541	0.129	1.9	2.0–6.3

[a] This is the only parameter which depends on the atomic weight of the stopping ion. The numbers are for ^{21}Ne.
[b] If a constant uncertainty of ϵ is assigned to the tabulation of Ref. 16, then a normalized χ^2 of unity is obtained in the fit to Eq. (2).
[c] The region of v/v_0 included in the fit for ^{21}Ne.

and Wright.[27] We consider an idealized monoenergetic, unidirectional beam of excited nuclei traveling in the z direction with initial velocity $v(0)$. The spreads in energy and direction which are inevitably encountered in practice are treated by assuming a skewed Gaussian distribution in velocity with the full width at half maximum (FWHM) and the skewness evaluated from the experimental conditions. We also assume a simple stopping medium, i.e., either stopping in the target or after exiting from a negligibly thin target. Deviations from this assumption are discussed in the Appendix. As the nuclei slow down they decay at the rate

$$dN(t)/dt = -(N_0/\tau)\exp(-t/\tau)\,, \tag{4}$$

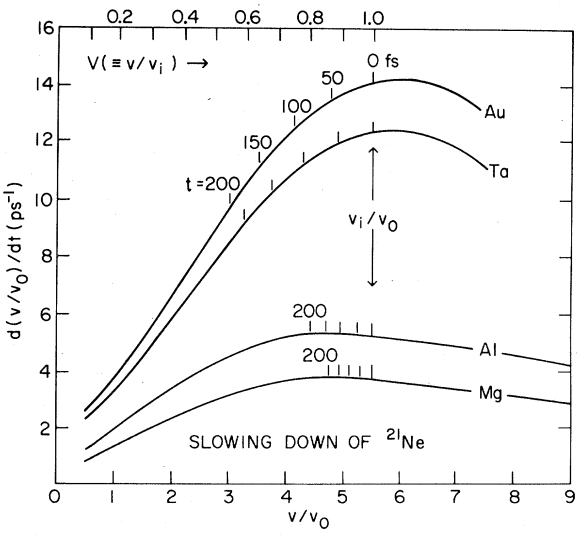

FIG. 2. Slowing power curves for ^{21}Ne ions in four materials. The slowing power is defined by Eq. (3). The top scale for V assumes an initial velocity $v_i/v_0 = 5.5$. For each curve the velocities corresponding to transit times of 0, 50, 100, 150, and 200 fs are indicated by vertical scribe marks. The effect of the magnitude of the slowing power on the rate of slowing down is apparent.

and there will thus be a continuous distribution of γ-ray energies $E_\gamma(t)$ between $E_{\gamma 0}[\equiv E_\gamma(\infty)]$ and $E_\gamma(0)$, where $E_{\gamma 0}$ is the energy of γ rays emitted by nuclei at rest, and $E_\gamma(0)$ is the energy of γ rays emitted at $t=0$ at an angle θ_γ to the z axis. The $E_\gamma(t)$ are given by the Doppler relation:

$$E_\gamma(t) = E_{\gamma 0}\{[1-\beta(t)^2]^{1/2}/[1-\beta(t)\langle\cos\theta_\gamma\rangle]\}\,, \tag{5}$$

where $\beta(t) = v(t)/c$ and $\langle\cos\theta_\gamma\rangle$ is the mean value of $\cos\theta_\gamma$. The extraction of the mean life τ from this line shape has been fully discussed previously.[12-14] The procedure used at this laboratory is based on the parametrization for $dE/d(\rho x)$ of Eq. (2) and is exemplified in Sec. III. Note that to first order Eq. (5) gives

$$E_\gamma(t) \simeq E_{\gamma 0}[1+\beta(t)\langle\cos\theta_\gamma\rangle]\,, \tag{6}$$

and so, to a very good approximation, the velocity line shape is also the γ-ray energy line shape and is directly observed.

For lifetimes very short compared to the stopping time of the ions, we can take the energy loss as constant,

$$-dE/d(\rho x) \equiv -M dv/dt = K_c(v_i/v_0)\,, \tag{7}$$

where the factorization of the constant to display the initial velocity $[v_i \equiv v(0)]$ is a convenience as should become apparent. Solving this differential equation gives

$$V = 1 - \alpha_c^{-1} t\,, \tag{8}$$

where $V \equiv v(t)/v(0)$ ranges from 1 to 0 as t varies from 0 to ∞ and $\alpha_c = Mv_0/\rho K_c$ is the characteristic slowing down time for the energy loss of Eq. (7). The velocity line shape corresponding to the energy loss of Eq. (7) is obtained using Eq. (4):

$$dN(V)/dV = x[e^{-x(1-V)} + x^{-1}\delta(V)e^{-x}]\,, \tag{9}$$

where $x = \alpha_c/\tau$. The ratio of the average Doppler shift to the maximum shift is termed the attenuation factor and is given by

$$F(\tau)=\int_0^1 V[dN(V)/dV]dV \Big/ \int_0^1 [dN(V)/dV]dV$$
$$=1-x^{-1}(1-e^{-x}). \quad (10)$$

For $\tau \ll \alpha_c$, i.e., large x, we have the useful relation

$$1-F(\tau) \underset{x\to\infty}{=} x^{-1}=\tau/\alpha_c, \quad (11)$$

which is, of course, true for any realistic expression for $-dE/d(\rho x)$. Note that the constant energy loss of Eq. (7) corresponds to the slowing power [cf., Eq. (3)]

$$d(v/v_0)/dt=\alpha_c^{-1}(v_i/v_0), \quad (12)$$

with $\alpha_c=227A_1/(\rho K_c)$ fs.

It is instructive to consider the very close analogy between the line shape of Eq. (9) and the distribution of time delays $\psi(t)$ encountered in an electronic timing measurement for a state of mean life τ. Such a timing measurement will have a prompt resolution function $P(t)$, and $\psi(t)$ is given by the convolution integral of $P(t)$ with the exponential decay [for a more detailed discussion of $\psi(t)$—usually termed $F(t)$—and $P(t)$ see Ref. 12]

$$\psi(t)=\int_0^\infty \tau^{-1}[\exp(-t'/\tau)]P(t-t')dt'. \quad (13)$$

Similarly, the experimentally observed line shape corresponding to the theoretical line shape of Eq. (9) will be

$$[dN(V)/dV]_{\rm exp}=\alpha_c\int_0^1 \tau^{-1}\{\exp[-\alpha_c(1-V')/\tau]\}$$
$$\times\phi(V-V')dV', \quad (14)$$

where $\phi(V-V')$ is the detector response function. We have suppressed the δ function part of Eq. (9) because it is negligible for $\tau \ll \alpha_c$ and, in any case, not relevant to the present discussion. It is seen that the analogy between the time distribution of Eq. (13) and the line shape of Eq. (14) is exact if we make the connection of variables between Eqs. (13) and (14) of $t\to 1-V$, $\tau\to\tau/\alpha_c$. [A more natural but completely equivalent connection would be $t\to\alpha_c(1-V)$, $\tau\to\tau$.] Once this connection is made it is a simple matter to apply the expertise and mathematical techniques developed for electronic timing to the DSA. For instance, there are two methods for extracting the lifetime from the distribution of time delays, $\psi(t)$, namely the slope and the centroid methods. In general, the slope method is more accurate but becomes less so as τ decreases until below some boundary value of τ, say τ_b, it becomes more accurate to determine τ from the centroid method. Likewise, lifetimes are extracted from the DSA by either line shape fitting or from the centroid of the line shape, i.e., from $F(\tau)$ *vis à vis* Eq. (11), and we wish to utilize results familiar from electronic timing to determine τ_b for the DSA.

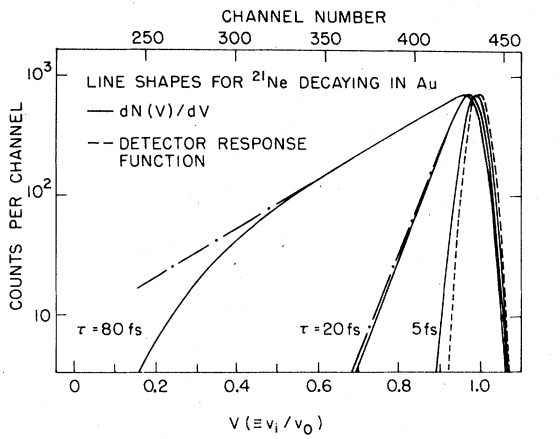

FIG. 3. Line shapes for ^{21}Ne decaying in Au. The theoretical line shape corresponding to the $-dE/d(\rho x)$ of Eq. (2) and Table II has been convoluted with the assumed detector response function indicated by the dashed curve. The resulting line shapes (solid curves) for $\tau=5$, 20, and 80 fs are indicated. The intensity scale for each is arbitrary. For 20 and 80 fs the dot-dashed curves have logarithmic slopes corresponding to 20 and 80 fs, respectively, and thus correspond to Eq. (14), i.e., to the assumption of a constant $-dE/d(\rho x)$. For 5 fs the dot-dashed and solid curves are undistinguishable. The logarithmic slopes were calculated using $\alpha_c=384$ fs.

Figure 3 shows line shapes for ^{21}Ne decaying in Au with $\tau=5$, 20, and 80 fs. The solid curves are the line shapes for the $dE/d(\rho x)$ of Eq. (2) as described by Warburton *et al.*[13] They were obtained by convolution with the Gaussian (assumed) detector response function illustrated by the dotted curve. First consider the fast lifetime limit for $dN(V)/dV$ given in Eq. (14). By analogy to electronic timing, we have[28]

$$\frac{d}{d(1-V)}[\ln G(V)]=-\frac{\alpha_c}{\tau}[1-\phi(V)/G(V)],$$

where $G(V)$ is shorthand for $[dN(V)/dV]_{\rm exp}$ and $\phi(V)$ in this case is given by $\phi(V)=\exp[-0.5(1-V)^2/\sigma^2]$. Thus in the velocity region where $\phi(V)\ll G(V)$, the logarithmic slope is a straight line and yields the mean life. Even if the assumption that $dE/d(\rho x)$ is constant breaks down (as is clearly the case for $\tau\gtrsim 20$ fs in Fig. 3), we still can say that $[dN(V)/dV]_{\rm exp}$ will yield accurate mean lives in the region of velocity where $\phi(V)\ll G(V)$. Once again, in analogy with electronic timing, we expect to be able to extract τ from the line shape if α_c/τ is $\gtrsim 1.3$ times the slope of the detector response function.[12] For a Gaussian response function, this criterion yields the boundary

value of τ

$$\tau_b \simeq 0.5\ (\mathrm{FWHM}/\Delta E_\gamma)\alpha_c\,, \qquad (15)$$

below which the mean life is most accurately obtainable from the centroid shift. In Eq. (15), the slope of the Gaussian is evaluated at $\frac{1}{2}$ maximum, and the FWHM is in keV as is the full energy shift $\Delta E_\gamma = E_\gamma(0) - E_\gamma(\infty)$. For Fig. 3, where FWHM = 6 keV and $\Delta E_\gamma = 112$ keV, we have $\tau_b \simeq 10$ fs.

III. RESULTS

A. The general experimental procedure

The inverse reaction ^{4}He(^{18}O, $n\gamma$)^{21}Ne ($Q_0 = -696$ keV) was used to form the ^{21}Ne levels under study. Targets were prepared by implanting ^{4}He$^+$ ions of 30–40 keV in thick blanks of Mg, Al, Ta, and Au to an areal density of ~4 μg/cm^2 as described in the Appendix. The use of ^{4}He-implanted targets in lifetime measurements via DSA line shape analysis has been developed and described by Forster and his co-workers at the Chalk River Laboratories[14] and applications to the measurement of the first-excited state of ^{22}Ne have been made at several laboratories.[29-31] However, only recently[32] has the method been applied to mean lives less than 100 fs. In a ^{4}He(^{19}F, $p\gamma$)^{22}Ne study of levels in ^{22}Ne up to 6817 keV, γ rays were observed[32] in coincidence with outgoing particles (as in all previous applications[14,29-31]) and only one stopping medium, Cu, was used. In rough conformity with the estimate given in Sec. II [Eq. (15)], a value of 15 fs was found for the fastest lifetime which could be measured in this DSA line shape study.

The present measurements differ from the ^{4}He(^{19}F, $p\gamma$)^{22}Ne measurements[32] just described in two important details. First, the recoiling ^{21}Ne ions were confined to a narrow cone near 0° and feeding from higher-lying levels was avoided by initiating the reaction near threshold rather than by observing γ rays in coincidence with light reaction particles. Second, by using four targets encompassing a wide range of stopping times, a relatively accurate lifetime could be obtained for the fast 2796-keV level [$\tau < \tau_b$—see Eq. (15)] from centroid rather than line shape analysis.

B. The 2796-keV level

1. The kinematics

Thin target excitation functions were recently obtained for formation of the 2789- and 2796-keV levels of ^{21}Ne via the ^{18}O(α, $n\gamma$)^{21}Ne reaction.[33] For the 2796-keV level the yield rises from the threshold at $E_\alpha = 4.27$ MeV to a strong complex resonance with a mean energy, $E_\alpha = 4.406$ MeV and an effective width of ~125 keV, and then falls to essentially a negligible cross section for $E_\alpha = 4.46$–4.56 MeV before rising again. The complex resonance is well fitted by a sum of two Breit-Wigner resonances with $(E_{R1}, \Gamma_1, \sigma_{R1}) = (4.384$ MeV, 82.6 keV, 6.04 mb); $(E_{R2}, \Gamma_2, \sigma_{R2}) = (4.441$ MeV, 30.2 keV, 10.1 mb). For bombardment of ^{4}He by ^{18}O the resonance energy parameters for the ^{18}O rest frame are multiplied by $\frac{18}{4} = 4.5$ and become $(E_{R1}, \Gamma_1) = (19.730$ MeV, 372 keV); $(E_{R2}, \Gamma_2) = (19.984$ MeV, 136 keV), with a mean energy and effective width of $(E_R, \Gamma) = (19.825$ MeV, 560 keV), respectively.

In order to interpret the DSA measurements it is necessary to know the mean energy at which the reaction takes place in the ^{4}He-implanted targets. (Some knowledge of the distribution of reaction energies is also desirable; however, this distribution contributes a minor amount to the total velocity distribution of the recoiling ^{21}Ne ions and so is not important.) The mean reaction energy is given by an energy-weighted convolution integral of the resonance with the ^{4}He density distribution. The depth of the ^{4}He in the targets and its density distribution were determined by excitation functions for the $\frac{1}{2}^-$ 2789-keV level. Details of these measurements and of the determination of the mean reaction energy are given in the Appendix, we only outline the procedures here.

Two sets of targets and of DSA measurements were made. In the first the targets were all made by implantation of 40-keV ^{4}He$^+$ ions and the same ^{18}O bombarding energy, $E(^{18}\mathrm{O}) = 20.1$ MeV, was used for all. For this set the mean reaction energy varied over 180 keV. In principle, a simple correction can be made for this variation; however, some systematic errors may be introduced by this procedure and so a second set of targets was made with the implantation energy adjusted in an attempt to obtain the same mean reaction energy for all targets. The subsequent excitation functions showed that this was not quite obtained; however, it was nearly accomplished by a small variation in bombarding energy from target to target. Finally, the very small adjustments needed to attain data corresponding to a mean reaction energy of 19.825 MeV were made via $dE_\gamma/(E_\gamma - E_{\gamma 0}) \simeq dv/v \simeq 0.5 dE_R/E_R$. This relationship was also used to adjust the results from the first set of targets.

The γ rays from the ^{21}Ne 2796 → 0 transition were detected by a 48.5-mm-diameter Ge(Li) detector at 0° to the beam axis and with its front face 10.5 cm from the target. The effective mean velocity of the recoiling ^{21}Ne* ions is given by

$$\beta(0) = \beta_{\mathrm{c.m.}}(1 + \gamma^{-1}\langle\cos\theta_{\mathrm{c.m.}}\rangle)\langle\cos\theta_\gamma\rangle\,, \qquad (16)$$

where $\beta_{\mathrm{c.m.}}$ and $\cos\theta_{\mathrm{c.m.}}$ are the velocity of the center of mass and the angle of the recoiling ^{21}Ne ions

in the center of mass, respectively. With the kinematical and experimental conditions described above, we obtain

$$\beta_{c.m.} = (3.978 \pm 0.028)\%, \qquad \gamma^{-1} = 0.0183 \pm 0.0043, \tag{17}$$

where the indicated excursions in $\beta_{c.m.}$ and γ^{-1} are those corresponding to a resonance width of 560 keV and are not uncertainties.

Averaging the γ-ray detection angle over the acceptance angle of the γ-ray detector gives $\langle\cos\theta_\gamma\rangle = 0.987 \pm 0.005$.[34] Inserting this value of $\langle\cos\theta_\gamma\rangle$ in Eq. (16) and assuming the reaction is symmetric about 90° in the center of mass with $\beta_{c.m.}$ from Eq. (17), yields

$$\langle \Delta E_\gamma / E_{\gamma 0} \rangle \equiv [E_\gamma(0) - E_{\gamma 0}]/E_{\gamma 0} = 4.004\% \tag{18}$$

for the mean fractional energy shift of the 2796-keV γ rays. For a γ-ray energy of $E_{\gamma 0} = 2795.64 \pm 0.7$ keV (see Sec. III B 3 below) we expect, from Eq. (18), a mean full Doppler shift, ΔE_γ, of 111.9 ±0.6 keV. The uncertainty is due almost entirely to that in $\langle\cos\theta_\gamma\rangle$. The second term on the right-hand side in Eq. (16) gives rise to a spread in ΔE_γ which we find is well-simulated by a Gaussian with a FWHM of 4.03 keV. In comparison the spread in reaction energies [see Eq. (17)] gives rise to a spread in ΔE_γ of ~1.5 keV.

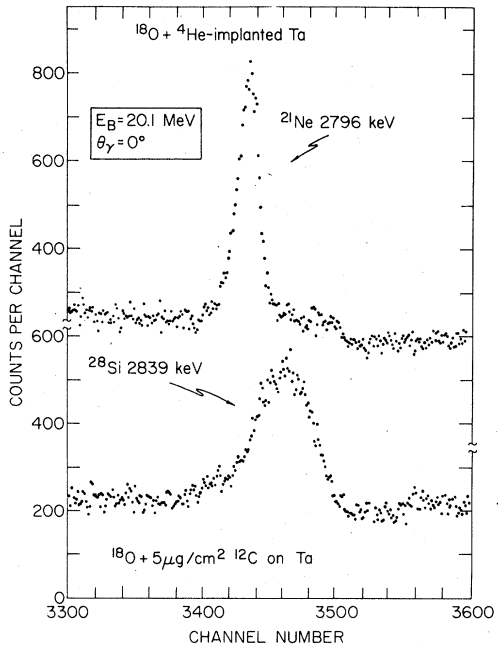

FIG. 4. Portions of γ-ray spectra obtained from 20.1-MeV ^{18}O bombardment of thick Ta with the γ-ray detector at 0° to the beam. The top spectrum was obtained with the ^{4}He-implanted target and the bottom spectrum from a target consisting of 5 μg/cm^2 of carbon evaporated onto a clean Ta blank. The energy dispersion is 0.49 keV/channel. The intensity scales of the two spectra are arbitrary.

2. *The measurement*

The ^{4}He-implanted targets were bombarded with ^{18}O ions of 20.1–20.6 MeV and with intensities of 150–300 nA of the 4$^+$ charge state. The beam spot was ~2 mm in diameter as defined by a collimator and observed by discoloration of the target after bombardment. The Ge(Li) cylindrical detector of 48.5-mm diameter was placed at 0° to the beam with its axis of symmetry on the beam axis and its front face 10.5 cm from the target. A ^{24}Na source was located near the target to provide an accurate energy reference in the Ge(Li) data. The detector efficiency was 16% relative to a 3×3-in. NaI(Tl) detector, and was also calibrated independently for γ-ray energies up to 2.614 MeV. To reduce the neutron flux, 6 cm of paraffin were placed between the target and detector. For each set of targets data were recorded using a 4096-channel analyzer for approximately 5 h per target. The net yield of the 2796-keV peak from the second set of targets averaged ~20% more than that of the first set. A major experimental difficulty was that the ^{12}C(^{18}O, $2n\gamma$)^{28}Si (4617 → 1779) reaction initiated on carbon impurities gave a background under the shifted 2796-keV γ ray. To minimize this effect care was taken in the ^{4}He implantation (see Appendix). Also, during the measurements, the vacuum in the beam line and target chamber was kept at 10^{-7} Torr and the target position was changed to obtain a new beam spot approximately every hour during the measurements. (The average yield for each beam spot served as an internal monitor on the local ^{4}He density.) The portion of the γ-ray spectrum displaying the shifted 2796-keV transition as obtained for the first Ta target is shown in Fig. 4. Also shown is a spectrum obtained from bombardment of a 5-μg/cm^2 ^{12}C target evaporated on a clean Ta blank. For each of the targets, the raw spectra were corrected for the ^{12}C background by subtracting such ^{18}O+^{12}C spectra, suitably normalized. Next, the shape and intensity of the Compton distribution, as determined from the nearby 2754-keV ^{24}Na(β^-)^{24}Mg γ ray, was subtracted. Finally, the remaining background, which displayed no noticeable structure near the ^{21}Ne peak, was subtracted assuming a first-order polynomial shape and using least-squares fitting to the regions just above and just below the ^{21}Ne peak. Representative spectra for the first set of Mg and Ta targets are shown in Fig. 5.

From the various measurements on the ^{21}Ne γ-ray spectra made during this investigation, an accurate energy determination of the ^{21}Ne 2789 → 0

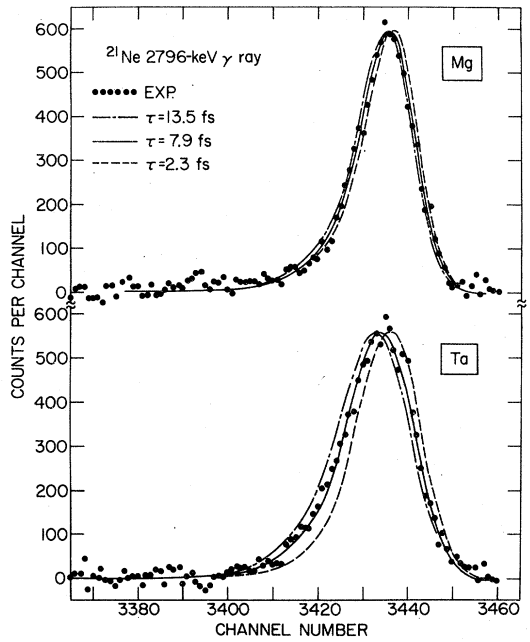

FIG. 5. The full-energy-loss peak of the ^{21}Ne 2796→0 transition observed at 0° to the beam after bombardment of ^{4}He implanted in Mg (top) and Ta (bottom). The energy dispersion is 0.49 keV/channel. Background and the counts due to the Compton distribution of the 2796-keV γ ray have been subtracted as described in the text. The theoretical line shapes, described in the text, are shown to illustrate the sensitivity of the results to the mean life τ of the 2796-keV level.

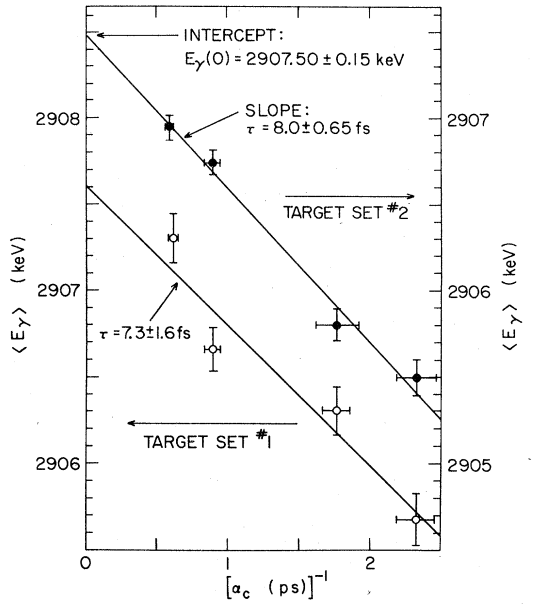

FIG. 6. Peak centroid versus inverse stopping time for the ^{21}Ne 2796-keV full-energy-loss peak observed following ^{18}O bombardment of ^{4}He implanted in Mg, Al, Ta, and Au. The data for the first and second sets of targets are displaced vertically and correspond to the energy scales indicated. The solid lines are least squares fits of Eq. (20) to the experimental points. The values obtained for $E_\gamma(0)$ and τ are indicated. These results were obtained neglecting the uncertainty in α_c^{-1}. The evaluation of the stopping time α_c, and the effect of this uncertainty, are discussed in the text.

transition was extracted. The 2789-keV level has a mean life of 117 ± 7 ps[4] and so the 2789-keV γ ray was not Doppler shifted in these measurements. The measurement was relative to the ^{24}Na γ ray of 2754.030 ± 0.014 keV[35] with the ^{24}Na γ ray of 1368.633 ± 0.006 keV[35] and the ^{1}H$(n,\gamma)^{2}$H γ ray of 2223.247 ± 0.016 keV[36] as secondary standards. The result was 2788.67 ± 0.10 keV corresponding to an excitation energy of 2788.87 ± 0.10 keV.

3. *Extraction of the mean life*

Briefly, the mean life τ of the 2796-keV level was extracted from a least-squares fit to the centroid of the 2796-keV line versus the inverse stopping time of ^{21}Ne in the four targets. That is, the attenuation factor $F(\tau)$ for the ith target is defined experimentally by

$$[F(\tau)]_i = [\langle E_\gamma^{(i)}\rangle - E_{\gamma 0}]/\Delta E_\gamma , \tag{19}$$

where $\langle E_\gamma^{(i)}\rangle$ is the energy centroid of the line shape distribution for the ith target. Combining Eqs. (11) and (19) we have

$$\langle E_\gamma^{(i)}\rangle = E_\gamma(0) - \tau \Delta E_\gamma [\alpha_c^{(i)}]^{-1} \tag{20}$$

for $\tau/\alpha_c \ll 1$. Thus a least-squares fit of a first-order polynomial to $\langle E_\gamma^{(i)}\rangle$ versus $[\alpha_c^{(i)}]^{-1}$ will yield an intercept corresponding to the full Doppler shifted energy $E_\gamma(0)$ and a slope of $-\tau\Delta E_\gamma$. Results of such a fit are illustrated in Fig. 6. The stopping times α_c were calculated as explained in Sec. II with a correction for the effect of the ^{4}He implantation on dv/dt as discussed in the Appendix.

The major uncertainty in the centroid energies $\langle E_\gamma^{(i)}\rangle$ of Eq. (19) and Fig. 6 arises from the background subtraction and is difficult to evaluate because it is due to the possible systematic deviation of the assumed background from the actual one. The uncertainty was estimated by varying the background subtraction procedures. That is, the relative intensity of the ^{12}C + ^{18}O background subtracted was varied, the remaining structureless background was represented by an exponential as well as a first-order polynomial, and, finally, the energy region included in the least-squares fit to determine the background was varied. The centroids were finally extracted by fitting to the channel region (see Fig. 5) 3408–3448 and the small correction for the omitted high- and low-energy tails of the line shape was carried out using

the theoretical line shapes. This procedure reduced considerably the sensitivity to the background subtraction and was estimated to introduce negligible error into the mean life extraction. An uncertainty of ±0.12(0.06) keV, corresponding to ±40(20) keV in the mean reaction energy, was added in quadrature to each uncertainty in the mean recoil energy determined in the first (second) set of measurements. The weighted average of the two values of $E_\gamma(0)$ and τ extracted from the fits illustrated in Fig. 6 were 2907.54 ± 0.15 keV and 7.9 ± 0.6 fs. Using the calculated ΔE_γ of 111.9 ± 0.6 keV we find a value of $E_{\gamma 0}$ of 2795.64 ± 0.7 keV or an excitation energy of 2795.84 ± 0.7 keV as compared to 2795.9 ± 0.6 keV quoted by Endt and Van der Leun.[5] The uncertainty in the mean life, $\tau = 7.9 \pm 0.6$ fs, is mainly due to that in the centroid energies and does not include a contribution from $dE/d(\rho x)$. Including our estimate of the uncertainty in $dE/d(\rho x)$—due almost entirely to the effects of the ^{4}He implantation (see Appendix)—results in a final value for the mean life of the 2796-keV level of 7.9 ± 1.0 fs. In both the line shape and centroid fitting procedures, second-order effects[12] were taken into account but were found to be negligible. For instance, the correction to τ for the β^2 term in the Doppler shift amounts to 2%.

Although the results just quoted could have been obtained without consideration of the γ-ray line shapes, it was felt desirable to investigate these line shapes for two reasons. First, as just discussed, knowledge of the theoretical line shape was helpful in obtaining as accurate energy centroids as possible. Secondly, a successful fitting of the line shapes greatly restricts the possibilities for undiscovered sources of systematic error. Line shapes similar to those of Fig. 3 were generated for each target. It was found that for $\tau < 10$ fs the shape of the γ-ray distribution for Mg was essentially independent of τ; that is, the only measurable effect of changing τ was to shift the distribution in energy. Thus, the experimental detector response function used was that of the Mg line shape. This shape had a FWHM consistent with that of the ^{24}Na 2754-keV line convoluted with the calculated kinematical spread of 4.03 keV. Using $E_\gamma(0) = 2907.54$ keV and a target density corrected for the ^{4}He implantation (see Appendix), the line shapes were calculated as illustrated in Fig. 5. For all targets normalized values of χ^2 close to unity were obtained for $\tau \sim 8$ fs. This was indeed reassuring; however, it should be emphasized that no one of the line shape fits by itself would have resulted in a meaningful measurement of τ. And, even taken all together, the line shape fits give an accuracy for the determination of τ inferior to that in the centroid fitting procedure—as long as the two procedures are applied independently. If, however, $E_\gamma(0)$ is determined from the centroids as in Fig. 6, then the line shape fits yield an average value for τ with comparable accuracy to the centroid procedure.

C. The 1747-keV level

As shown in Fig. 1, the ^{21}Ne $\frac{7}{2}^+$ 1747-keV level decays 95% to the 351-keV first-excited state. The line shape of the 1396-keV 1747 → 351 transition was observed with good statistics, for all four implanted targets, in the same spectra recorded for study of the 2796-keV level. The line shapes were analyzed in a fashion similar to that described for the 2796-keV transition except that the Compton distribution was not subtracted, but was instead included as part of the detector response function. The background was structureless except for the ^{40}Ar(β^-)^{40}K 1461-keV γ ray just above the line shape and the second-escape peak of the ^{21}Ne 2789 → 0 transition in the center of the line shape. Both were subtracted utilizing their known shapes and normalizing the intensity of the second-

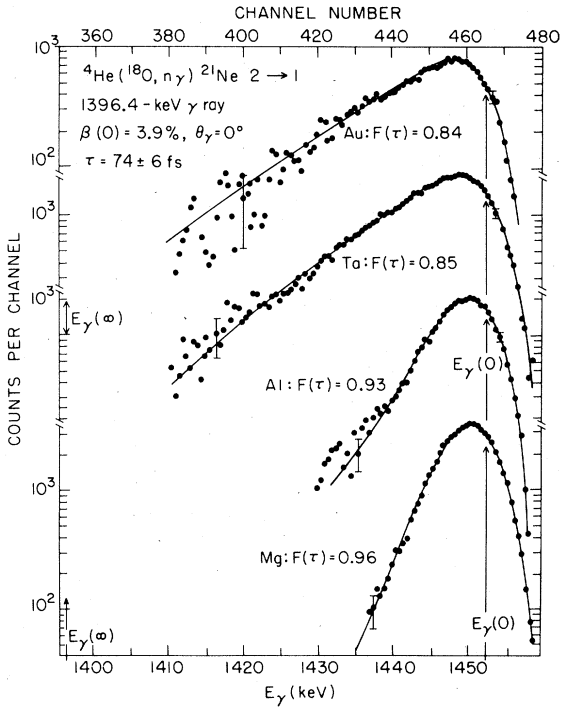

FIG. 7. Line shapes observed for the ^{21}Ne 1747 → 351, 1396-keV transition following ^{18}O bombardment of ^{4}He implanted in Mg, Al, Ta, and Au. The attenuation factor $F(\tau)$ is shown for each target as is the full Doppler shifted energy obtained from a fit similar to that of Fig. 6. The theoretical fits are described in the text.

escape peak of the 2789-keV transition to that of its full-energy-loss peak. The resulting line shapes for the first set of targets are shown in Fig. 7. There is no feeding from higher-lying levels since the only ones formed—the 2789- and 2796-keV levels—do not decay to the 1747-keV level. The cross section for the 1747-keV level was also found to be resonant at $E(^{18}O) \simeq 19.825$ MeV, and the fractional Doppler shift was also calculated to be 4.004% for the 1396-keV γ ray [see Eq. (19)]; however, because the reaction is further from threshold than for the 2796-keV level, the kinematical spread is considerably more. It was found to be well simulated by a Gaussian with FWHM = 5.3 keV as compared to the detector response with FWHM = 4.4 keV.

As a first step in the extraction of τ, the full Doppler-shifted energy $E_\gamma(0)$ was extracted from a fit of Eq. (20) in a manner similar to that illustrated in Fig. 6, with the result $E_\gamma(0) = 1452.3 \pm 0.1$ keV. Subtracting the expected shift $\Delta E_\gamma = 55.9 \pm 0.3$ keV, yields $E_{\gamma 0} = 1396.4 \pm 0.3$ keV as compared to the value of 1394.83 ± 0.20 keV expected from the compiled excitation energies.[5] The agreement is very poor. We note that Grawe *et al.*[6] obtained $E_{\gamma 0} = 1396.4 \pm 0.4$ keV for the 1747 $\rightarrow$ 351 transition and this value is not included in the set used to obtain the compiled[5] excitation energies. The excitation energy of the 1747-keV level corresponding to $E_{\gamma 0} = 1396.4 \pm 0.3$ keV is 1747.2 ± 0.3 keV using 350.72 ± 0.06 keV[5] for the first-excited state.

In the centroid fit to Eq. (21), which yielded $\tau = 70 \pm 6$ fs, the modification of the stopping times $\alpha_c^{(i)}$ due to the ^{4}He implantation was estimated only roughly. In addition, the approximation of a constant $dE/d(\rho x)$ introduces some uncertainty because $\alpha_c \gg \tau$ is not well satisfied. Thus, the final and best value for τ was obtained from the line shape fits shown by the solid curves in Fig. 7. After the preliminary fits to check on the kinematical conditions, the mean life τ was obtained from a fit to the slope of the line shape in the energy region below the peak. That is, the fit was confined to the region of channels < 455 shown in Fig. 6. This corresponds to flight times > 130 fs or distances > 1.56 μm which is well beyond the implanted region (see the Appendix). As explained at the end of Sec. II, the result so obtained is insensitive to the detector response function and, most importantly, the ^{21}Ne recoils are out of the ^{4}He-implantation region and decaying in the target with well-known density and $dE/d(\rho x)$. The final average value[37] for the four backing materials obtained for the mean life of the 1747-keV level was

$$\tau = 74 \pm 6 \text{ fs}.$$

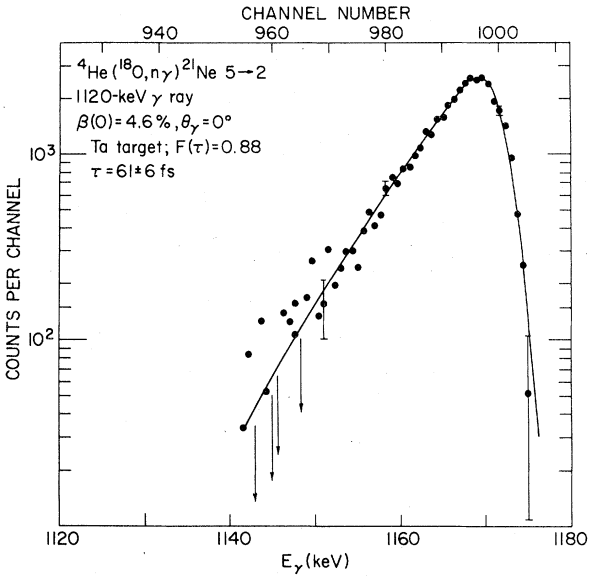

FIG. 8. Line shape observed for the ^{21}Ne 2867 $\rightarrow$ 1747, 1120-keV transition following ^{18}O bombardment of ^{4}He implanted in Ta. The theoretical fit is described in the text.

D. The 2867-keV level

The ^{21}Ne $\frac{9}{2}^+$ 2867-keV level decays 62% to the 1747-keV level with[5] $E_{\gamma 0} = 1120.0 \pm 0.3$ keV (see Fig. 1). This γ ray was not observed with enough intensity for a line shape analysis for ^{18}O bombarding energies below 24 MeV. At energies above ~24 MeV γ rays from ^{18}O + ^{24}Mg and ^{18}O + ^{27}Al fusion evaporation and transfer reactions became very intense relative to the ^{18}O + ^{4}He intensities. Therefore, shapes were obtained only for the Ta and Au targets and because the results for Au had poor statistics only the Ta measurements was analyzed. The line shape for Ta was meaured at $E(^{18}O) = 27$ MeV and is shown with background subtracted in Fig. 8. The theoretical fit is for $E_\gamma(0) = 1171.1$ keV corresponding to a full Doppler shift of 51.1 keV or 4.56%. As in the case of the 1747-keV level the mean life was obtained from the slope of the line shape in the region where the dependence on kinematics, the detector response, and the effects of the ^{4}He implantation are minimal. That is, for the line shape of Fig. 8 the fit was confined to channels 960–997. A result of 61 ± 6 fs was obtained for the 2867-keV level.

IV. DISCUSSION

A. Comparison with previous methods

We have presented in this report a method for measuring fast lifetimes based on implanted targets and the high-velocity DSA. The result for the

2796-keV level is more accurate than obtained in any previous DSA measurements of $\tau < 10$ fs lifetimes. The success of this extension of precision DSA results to fast lifetimes is due mainly to the use of implanted targets. Their use allows a wide choice of stopping materials and, by stopping the recoils in the target itself, uncertainties in the target thickness are avoided. These two factors—use of several stopping materials with a wide range of slowing times and stopping in the target itself—were crucial to the accuracy of the method for the fast lifetime. A vexing source of uncertainty is that due to the uncertainties in dv/dt associated with the ^{4}He implantation. It is hoped that future studies of the implantation process can reduce the uncertainty associated with this effect.

For the two slower lifetimes, these two factors are not nearly as important. Here, our accuracy is essentially the same as previous high precision DSA results, e.g., Refs. 21, 32, and 38. Important to the accuracy obtained were the higher statistics made possible because the coincidence technique was avoided. One important contribution we made to the $\tau = 20$–100 fs region was to avoid the uncertainty due to the effect of ^{4}He implantation on the slowing time by fitting to a restricted region of the line shape.

There are two alternative DSA techniques which have successfully yielded fast lifetime measurements and it is instructive to compare them to the present technique.

The method of Branford and Wright. This experimental method[27] uses heavy-ion induced reactions, e.g., ^{12}C(^{16}O, α)^{24}Mg and particle-γ coincidences. The essence of the technique is to compare the attenuation factor $F(\tau)$ observed for a thin unbacked target to that observed for a backed target. The analysis is quite similar to that presented in Sec. II and the recoil velocities are comparable to those of the present study. This technique is in some respects more versatile and efficient than the present one. Versatile because most nuclei not too far from stability can be formed in high cross-section heavy-ion fusion-evaporation or transfer reactions and efficient because the coincidence technique allows the study of many levels simultaneously. However, the difficulty of fabricating thin targets of known thickness and suitable for heavy-ion bombardment limits the versatility of the method. The sensitivity to the target thickness—as exemplified by the discussion below (Sec. IV B 1) of the results of Grawe *et al.*[6]—and the poor statistics engendered by the coincidence requirement are the major reasons why we feel this technique is intrinsically of poorer accuracy for $\tau < 10$ fs than the present one. However, when carefully applied it is capable of nearly comparable accuracy, for instance, Wright, Cooke, Fifield, and Poletti[27] quote 6.2 ± 1.6 fs for the mean life of the ^{24}Mg 8.11-MeV level obtained in ^{12}C(^{16}O, α)^{24}Mg. The technique is complementary to the present one.

The method of Anttila and Bister. In a series of studies[39,40] of nuclear lifetimes utilizing implanted targets and the resonant (p,γ) reaction, Anttila, Bister, and co-workers have developed the low-velocity DSA to an accuracy comparable to that of the present method. In a typical study,[40] a ^{13}C target was made by implanting ^{13}C in Ta and the $F(\tau)$ values of various ^{14}N γ transitions were measured using the ^{13}C$(p,\gamma)^{14}$N reaction at the $E_p = 1.15$-MeV resonance. For this case $\beta = 0.36\%$ and dv/dt is dominated by nuclear scattering. The high accuracy depends on the very large magnitude of dv/dt encountered for such small velocities and on a careful Monte Carlo treatment of the nuclear scattering. The resultant accuracy is also aided by good kinematical conditions and a clever scheme of experimental conditions. Although the analysis is carried out with great care, the nuclear scattering is not well understood theoretically and there is some possibility of systematic uncertainties larger than those estimated.

B. Comparison with previous results

The published mean life measurements for the three ^{21}Ne levels under study are compared to the present results in Table III. All four previous measurements were via the DSA method. One other result for the 1747-keV level, derived from Coulomb excitation,[5,41] is omitted since the measurement was performed too high above the Coulomb barrier to be reliable.[21]

1. The results of Grawe et al.

The only previous mean life determination for the 2796-keV level—the main focus of the present study—was the high-velocity inverse ^{2}H(^{20}Ne, p)^{21}Ne reaction study of Grawe *et al.*[6] In that measurement γ rays were observed at 45° and 135° to the 21-MeV ^{20}Ne beam in coincidence with protons observed near 0° to the beam. The attenuation factor $F(\tau)$ was then obtained as the ratio of the observed Doppler shift to that calculated from the kinematics and detection geometry for $\tau = 0$. The target consisted of 50 μg/cm^2 of deuterated polyethylene evaporated onto Ta. In our opinion, the experiment and its analysis contain uncertainties of sufficient severity to invalidate the conclusion for the 2796-keV level and to increase somewhat ($\gtrsim 10\%$) the uncertainties assigned to the mean lives of the 1747- and 2867-keV levels. The sources of uncertainty in question are the following:

TABLE III. Comparison of present and previous lifetime results for ^{21}Ne.

E_x (keV)	Present	τ (fs) ^{9}Be(^{16}O,α)[a]	^{18}O(α,n)[b]	^{18}O(α,n)[c]	^{2}H(^{20}Ne,p)[d]
1747	74 ± 6	150 ± 130	76 ± 12 (76 ± 20)	24 ± 6	85 ± 7 (85 ± 11)
2796	7.9 ± 1.0		<27	···	10 ± 4 (<20)
2867	61 ± 6	110^{+150}_{-70}	56 ± 14 (56 ± 18)	27 ± 5	50 ± 12 (50 ± 13)

[a] Reference 8; $\beta = 2.1$, Na(Tl) detectors.

[b] References 9, 10; $\beta \simeq 1.0\%$. The uncertainties assigned to the results are experimental only. The results in parentheses are our revisions obtained by adding 15%, 10%, and 10% for $dE/d(\rho x)$, ρ, and the analysis as explained in the text.

[c] Reference 11; $\beta \simeq 1.0\%$. See text.

[d] References 6, 7; $\beta \simeq 4\%$. The results in parentheses are our revisions as explained in the text.

(1) For $\beta = 4\%$ the flight time of the ^{21}Ne recoils through a 50-μg/cm^2 ($\rho \simeq 1$ g/cm^3) target is ~40 fs. Thus, for $\tau = 10$ fs 76% of the recoils decay in the target which has a dv/dt 2.5 times smaller than that of Ta. Thus, not only is the measurable effect, $1 - F(\tau)$, commensurately smaller than for decay in pure Ta, but the result is also very sensitive to the time spent in the target. (Incidentally, this difficulty illustrates the main limitation to the accuracy of the technique of Branford and Wright.[27]) During the measurement the yield was observed to decrease by a factor of 5, while a subsequent measurement indicated the areal density of the target was the same after the measurement as before, to an accuracy of 10%. This was interpreted to indicate a loss of deuterium only, leaving the stopping power almost unchanged. No uncertainty was explicitly assigned to τ from this source. It is our contention, however, that a change in density would almost certainly accompany such a drastic change in composition: Then, because the areal density is essentially unchanged, the thickness and thus the average flight time and the fraction of recoils decaying in the target would be directly affected. This could be a quite large effect because the density of carbon is ~twice that of polyethylene. An accounting for the effect could lead to a decrease in the extracted mean life by up to 50%.

(2) The calculated full Doppler shift (FDS) in the measurement of Grawe *et al.*[6] is of the form

$$\mathrm{FDS}_{\mathrm{calc}} = E_{\gamma 0}\beta[Q_1(45°)\cos 45° - Q_1(135°)\cos 135°], \quad (21)$$

where the geometrical factors—in square brackets—are displayed explicitly because we wish to discuss their assigned uncertainties. That is, there will be contributing errors to $\mathrm{FDS}_{\mathrm{calc}}$ from possible deviations from 45° and 135°, i.e., in cos45° and cos135° and also from uncertainties in the solid-angle attenuation coefficients[34] $Q_1(45°)$ and $Q_1(135°)$. For the 2796-keV level Grawe *et al.* give $\mathrm{FDS}_{\mathrm{calc}} = 148.0 \pm 0.2$ keV or a 0.14% uncertainty. Yet they quote $Q_1(45°) = 0.957 \pm 0.005$ which gives rise to a 0.26% uncertainty or ±0.38 keV all by itself. The contributing uncertainties of cos45°, cos135°, and $Q_1(135°)$ are not given by Grawe *et al.*, but certainly are not negligible especially in view of the small detector-target distance, 6.2 cm.

For these two reasons we feel that the measurement of Grawe *et al.*[6] on the mean life of the 2796-keV level should be interpreted as an upper limit, $\tau < 20$ fs, and that the uncertainties assigned by Grawe *et al.* to the mean lives of the 1747- and 2867-keV levels are too conservative. We suggest a 10% additional contribution and this is indicated in Table III.

2. *The results of Bailey et al.*

The comparison of Table III indicates quite strongly that the results of Bailey *et al.*[11] are systematically too low. A clue to the origin of a systematic error in the DSA study of Bailey *et al.* is that an attenuation factor $F(\tau) = 0.046 \pm 0.002$ was observed for the ^{21}Ne 351 → 0 transition yielding $\tau = 3.6 \pm 0.3$ ps, while the mean life of this state (as reviewed by Millener *et al.*[4]) is 10.18 ± 0.16 ps for which $F(\tau) \simeq 0.017$ would have been expected. One possible explanation of this discrepancy is the presence of voids in the evaporated WO_3 target used in these measurements so that the ^{21}Ne recoils decay partially in vacuum. If voids were present the relationship between τ and the effect of the voids would depend on their nature (size) but would reasonably be expected to be larger for 50–100 fs than for 10 ps.

3. The results of Rolfs et al.

The results of Rolfs *et al.*[9] are a re-analysis, using the Blaugrund[42] approach, of the original mean life results of Pronko *et al.*[10,43] We have repeated this re-analysis using the Blaugrund approach and find essential agreement with the mean lives quoted by Rolfs *et al.* (Table III).[44] The uncertainties assigned by Rolfs *et al.* (Table III) account only for the experimental errors on the $F(\tau)$. The uncertainties in parenthesis in Table III include additional estimates of 15% due to $dE/d(\rho x)$, 10% due to the uncertain target composition and density, and 10% to the inadequacies of the Blaugrund treatment.

C. Comparison with shell-model predictions

The present results are compared to shell-model predictions of Millener[45] in Table IV. This calculation, performed in a SU3 basis, uses an inert s^4p^{12} core and a full $(sd)^5$ space. Results are shown in Table IV for two effective interactions, Kuo-Brown (KB)[46] and Chung-Wildenthal (CW)[47]. The $B(M1)$ were calculated with the bare nucleon g factors and the $B(E2)$ using oscillator radial wave functions with the size parameter b fixed at 1.784 fm. An additional charge ϵ such that $e_p = (1+\epsilon)e$ and $e_n = \epsilon e$ was assumed in the calculations of the $B(E2)$ values: the two entries for $B(E2)$ in Table IV are for $\epsilon = 0.5$ and 0.35, with the latter in parenthesis. Table IV supplements results already given[49] for the Kuo-Brown interaction with $\epsilon = 0.5$. The overall agreement between theory and experiment is remarkably good. It is perhaps somewhat better for the Kuo-Brown interaction than for the Chung-Wildenthal interaction, but the difference is hardly significant. In the Nilsson model, the ^{21}Ne $\frac{3}{2}^+$, $\frac{5}{2}^+$, $\frac{7}{2}^+$, and $\frac{9}{2}^+$ levels are described as members of a $K_J = \frac{3}{2}$ band built on an intrinsic state with four particles filling the No. 6 orbit and one particle in orbit No. 7. This

TABLE IV. Comparison of experiment to shell-model predictions for electromagnetic transitions between the lowest five even-parity states of ^{21}Ne.

Transition $J_i^\pi \to J_f^\pi$	Quantity[a]	Theory[b] KB[c]	Theory[b] CW[d]	Experiment[e]
$\frac{5}{2}^+ \to \frac{3}{2}^+$	$B(M1)$	0.084	0.089	0.072 ± 0.001
	$B(E2)$	28(20)	27(19)	24 ± 3
	$x(E2/M1)$	+0.074	+0.071	+0.074 ± 0.005
	τ (ps)	8.7	8.3	10.18 ± 0.16
$\frac{7}{2}^+ \to \frac{3}{2}^+$	$B(E2)$	12(9)	11(8)	9.7 ± 1.9
	τ (ps)	1.2	1.3	1.5 ± 0.3
$\frac{7}{2}^+ \to \frac{5}{2}^+$	$B(M1)$	0.13	0.18	0.15 ± 0.01
	$B(E2)$	21(15)	20(15)	11 ± 3
	$x(E2/M1)$	+0.20	+0.17	+0.14 ± 0.02
	τ (fs)	87	63	78 ± 6
$\frac{1}{2}^+ \to \frac{3}{2}^+$	$B(M1)$	0.27	0.13	0.20 ± 0.014
	$B(E2)$	1.3(0.88)	0.57(0.40)	...
	$x(E2/M1)$	−0.071	−0.068	...
	τ (fs)	5.3	11.3	7.9 ± 1.0
$\frac{9}{2}^+ \to \frac{5}{2}^+$	$B(E2)$	16(12)	15(11)	15 ± 1.6
	τ (fs)	145	155	160 ± 18
$\frac{9}{2}^+ \to \frac{7}{2}^+$	$B(M1)$	0.22	0.25	0.23 ± 0.02
	$B(E2)$	11(8)	11(8)	9 ± 5
	$x(E2/M1)$	+0.09	+0.09	+0.08 ± 0.02
	τ (fs)	102	89	98 ± 10

[a] The transition strengths, $B(EL)$ and $B(ML)$, are in Weisskopf units (Ref. 48), the mixing ratios $x(L+1/L)$ are dimensionless, and the units for the mean lifetimes, τ, are given.

[b] D. J. Millener, see text. The $B(E2)$ values are given for effective charge parameters of $\epsilon = 0.5$ and 0.35, with the latter in parentheses. The mixing ratios and partial lifetimes were calculated using the experimental excitation energies and $\epsilon = 0.5$.

[c] Using the Kuo-Brown interaction (Ref. 46).

[d] Using the Chung-Wildenthal interaction (Ref. 47).

[e] The mixing ratios are from Ref. 5. The partial mean lives are based on the adopted branching ratios of Fig. 1 (from Ref. 5) and the present total mean lives. The $B(M1)$ and $B(M2)$ values are calculated from the mixing ratios and the partial mean lives. The $\frac{1}{2}^+ \to \frac{3}{2}^+$ branching ratio is assumed to be 100%. For the $\frac{5}{2}^+ \to \frac{3}{2}^+$ transition the results are as given in Ref. 4.

description is remarkably successful. Thus, the good theoretical description of the electromagnetic transitions connecting these states is not surprising. To a very good approximation, they all have the same basic structure[50] and the $M1$ and $E2$ transitions connecting them are essentially determined by gross properties of the nuclear structure and are not sensitive to small changes in the wave functions.

The most sensitive parameter in Table IV is the $B(M1)$-value (and thus τ) for the $\frac{1}{2}^+ \rightarrow \frac{3}{2}^+$ transition. The measured value lies between that for the Kuo-Brown and Chung-Wildenthal interactions. In a SU3 basis the $\frac{3}{2}^+$ state is largely [41] (81) with [41] (62) next in intensity (of order 10%),[4] while for the $\frac{1}{2}^+$ state, these intensities are reversed. The spin part of the $M1$ matrix element, which is intrinsically larger than the orbital part and dominates the $\frac{1}{2}^+ \rightarrow \frac{3}{2}^+$ $M1$ matrix element is essentially due to the (81) $\rightarrow$ (81) piece. Examination of the contributions to the $M1$ matrix element reveals that the difference in $M1$ rates for the KB and CW interactions is due to a large change in the relative intensity of the (81) component in the $\frac{1}{2}^+$ state. It is 12% in intensity using the KB interaction and 5.6% using the CW interaction. The reason for this large difference is not immediately obvious; but since the second $\frac{1}{2}^+$ state of $(sd)^5$ is largely (81), it reflects a difference in a mixing of the two lower $\frac{1}{2}^+$ states in the two interactions. We note then that the experimental $B(M1)$ for the $\frac{1}{2}^+ \rightarrow \frac{3}{2}^+$ transition, being senstive to the amount of (81) in the $\frac{1}{2}^+$ state, can be thought of as determining it.

The predicted $B(E2)$ values tend to give better agreement for $\epsilon = 0.35$ than for $\epsilon = 0.5$. This is in agreement with the omnibus sd shell comparison of Schwalm *et al.*[21] who found that the best overall agreement between the Chung-Wildenthal interaction and experiment for the $B(E2)$ values of low-lying transitions in the range $20 \leq A \leq 37$ was obtained with an effective charge parameter of $x = 0.35$ using $b = 1.072A^{1/6}$ fm (which for $A = 21$ yields $b = 1.781$).

As stated in the Introduction, the main motive for this study was to provide a value for the $B(M1)$ of the $\frac{1}{2}^+ \rightarrow \frac{3}{2}^+$ transition accurate enough for use in the evaluation of the to-be-measured parity nonconserving matrix element. A secondary motive was to provide further data for the testing of shell-model calculations so that the predictions[4] relating to the parity nonconserving matrix element can be made with more confidence. The successful accomplishment of these objectives demanded the further development of the DSA method for use with implanted targets and fast lifetimes. Since a careful examination of all facets of the measurement and analysis was a necessary part of the attained accuracy, these were described in some detail. The method described should be capable of higher accuracy than presently attained and is applicable to a number of measurable lifetimes in the 1–100-fs range.

ACKNOWLEDGMENTS

This research was supported by the Division of Basic Energy Sciences, Department of Energy, under Contract No. EY-76-C-02-0016. We would like to thank A. Goland and J. S. Rosner (BNL), R. A. Johnson (U. Va.), and R. Wilson (Sandia Corp.) for discussions concerning the implantation of ^{4}He in matter, D. J. Millener who provided us with results of his shell-model calculations and discussed them with us, T. K. Alexander for information regarding his DSA measurements on ^{22}Ne prior to publication, and D. Schwalm (GSI) for several helpful discussions.

APPENDIX: ^{4}He-IMPLANTED TARGETS FOR DSA MEASUREMENTS

The utilization of light-ion implanted targets for DSA measurements of nuclear lifetimes has been reported by numerous investigators, and representative examples illustrating the implantation of noble gases in metals of $A > 48$ are specifically cited.[29-32,39-40,51] Experimental data on the characteristics of these targets—such as the relative concentrations and distributions of the implanted ions—have also been presented.[29,39-40,51-55]

Most of the precision DSA measurements thus far reported are for relatively longer lifetimes ($\tau \geq 50$ fs). For such cases the mean decay distance of the recoil excited nucleus is appreciably greater than the spatial thickness of the implanted target layer, and the approximation is therefore quite well justified that the slowing power, dv/dt, is that of the pure host material. Or, as in the present analysis for the 1747- and 2867-keV levels, the approximation can be avoided by excluding that part of the line shape corresponding to decay in the implanted region. However, the application of the DSA technique to the measurement of shorter nuclear lifetimes (say $\tau \lesssim 20$ fs) is not so well understood because of the questions which arise as to the value of dv/dt appropriate to the implantation region. The nature of the problem can be most easily understood from a preliminary consideration of the present measurements for ^{21}Ne in the ^{4}He-implanted targets. For γ emission from a ^{21}Ne state of $\tau \sim 8$ fs, the mean decay distance is $v\tau \simeq 0.10$ μm, a distance which is of the order of the spatial thickness (0.1–0.4 μm) of the ^{4}He distribution in the implanted target metals.

The stopping time α_c, which is the critical energy-loss parameter [see Eq. (11)], is therefore influenced by the presence of the ^{4}He-implanted atoms and must be taken into account explicitly.

In this Appendix we begin by describing the mechanical details of the target preparation. Experimental measurements of known resonance structure[33] in the ^{4}He(^{18}O, $n\gamma$)^{21}Ne reaction were employed to deduce the spatial distribution and atomic concentration of the ^{4}He implanted in the various host metals. These results were compared and found to be in satisfactory agreement with the ^{4}He profiles expected from simple calculations based on transport theory. Finally, we have attempted to account, in a quantitative way, for the resultant influence on dv/dt due to the implantation process.

1. Preparation of ^{4}He-implanted targets

Targets of high purity (> 99.9%) natural Mg, Al, Ta, and Au were implanted with ^{4}He$^+$ ions using a HVEC duoplasmatron ion source operated at extraction voltages providing selected energies $E(^4\text{He}) \leq 45$ keV. Target blanks of thickness 250–500 μm were first etched to remove surface contaminants and then covered by a thin ($\leq$15 μg/cm^2) protective layer of evaporated NaCl. The blanks were clamped to a brass target holder which maximized heat conduction from the implantation area such that the surface temperature did not exceed ~100 °C. The implantations were accomplished by ~1 h bombardments using 20–30 μA beams of ^{4}He$^+$ ions, which were deliberately defocussed over a cross-sectional area of 1.0 cm^2. This provided typical implantation doses of $\sim 6 \times 10^{17}$ He-atoms/cm^2 corresponding to an areal density of ~4 μg/cm^2 of ^{4}He. The ^{4}He bombardment was done in a high-vacuum environment ($< 2 \times 10^{-7}$ Torr) in order to reduce the deposition of contaminant impurities on the target site. After implantation, the NaCl layer was washed away, removing all visible traces of a very slight carbon buildup.[56]

Two sets of targets were prepared in this way. The first set was made at a uniform ^{4}He bombarding energy of 40 keV for a net incident bombardment dose (Φ_{inc}) of 6.7×10^{17} ^{4}He-atoms/cm^2 for each target. The energy loss in the 10-μg/cm^2 NaCl layer was ~6 keV, so that the ^{4}He energy incident on the metal surface was actually ~34 keV. Because the ranges of ^{4}He in different metals vary considerably, this procedure resulted in targets implanted to varying depths, introducing minor but undesirable complications into the measurement and analysis of the DSA data, as discussed in the main text.

At a later date, therefore, a second set of targets was prepared in which the ^{4}He bombarding energies were calculated to provide implantations to a depth corresponding to a uniform ^{18}O energy loss [for $E(^{18}\text{O}) \sim 20$ MeV] of ~420 keV for all targets. With these targets the $F(\tau)$ measurements could all be made using nearly the same ^{18}O energy to populate the ^{22}Ne resonant states leading to the ^{21}Ne 2796-keV level. The measurements with this second set of targets provided a more accurate determination of τ, in part because the statistics and signal/background ratio were better, and also because the uniform implanted depth reduced the possibilities for systematic errors in the analysis. In the following we therefore describe in detail the analysis to determine the character of the targets used in the second set of measurements, noting that a similar analysis for the first set was also satisfactorily accomplished.

2. Distribution of the implanted ^{4}He ions

Pertinent data on the ^{4}He-implanted targets used in the second set of DSA measurements are collected in Table V. For each target the crystalline structure and density are indicated, as well as the ^{4}He bombarding energies [$E(^4\text{He})$] and dose [Φ_{inc}] used in the target implantations. The loss in the NaCl protective layer at these ^{4}He energies is ~0.6 keV cm^2/μg, so that the ^{4}He energies incident on the metals are lower than the tabulated values of $E(^4\text{He})$ by 6–9 keV.

Yield curves for the ^{4}He(^{18}O, $n\gamma$)^{21}Ne reaction were measured at $\theta_\gamma = 90°$ for each of the eight implanted targets, using a calibrated Ge(Li) detector. Pertinent data for the second set of targets, showing the intensity of 2438-keV γ rays resulting from de-excitation of the ^{21}Ne $J^\pi = \frac{1}{2}^-$ state, are shown as a function of ^{18}O bombarding energy in Fig. 9. The data have been fitted with Gaussian shapes to extract the apparent resonance energies (E_r') and resonance widths (Γ_r'). In order to ascertain the uniformity of the target implantation, the resonant yield of 351-keV γ rays was measured as the ^{18}O beam was scanned across the diameter of the target spot. The results, shown in the insets, indicate a satisfactorily flat radial density distribution of ^{4}He.

Absolute cross sections for the ^{18}O(^{4}He, n)^{21}Ne* reaction have been measured by Switkowski *et al.*[33]; these data have been scaled for the inverse reaction ^{4}He(^{18}O, n)^{21}Ne* and are shown in the upper plot of Fig. 9. The data have been fitted with Breit-Wigner shapes to determine the "true" resonance energy E_r and width Γ_r for the $J^\pi = \frac{1}{2}^-$ state, as given in Fig. 9.

From the yield curve data for the ^{4}He-implanted targets, the displacement of the apparent reso-

TABLE V. Summary of parameters specifying the character of the ^{4}He-implanted targets used in the second set of DSA lifetime measurements. The first 4 columns list pertinent details for the host metal. The next 3 specify details of the implantation, at bombarding energies $E(^4\text{He})$, where Φ_{inc} is the areal density of the integrated ^{4}He flux. The last columns are experimental values deduced from the data of Fig. 9, giving the range and width parameters R_z and ΔR_z, the areal density Φ of the ^{4}He *retained* in the metal, and the ^{4}He atomic concentration C_0 corresponding to the peak of the implanted distribution.

	Target			Implantation			Distribution of ^{4}He in metal (Experimental data)			
Metal	(Crystal type)[a]	Density (g/cm^3)	$\frac{dE}{d(\rho x)}(^{18}\text{O})$[b] (keV $cm^2/\mu g$)	$E(^4\text{He})$ (keV)	NaCl[c] thickness ($\mu g/cm^2$)	$\Phi_{\text{inc}}(^4\text{He})$ (10^{17} atom/cm^2)	R_z ($\mu g/cm^2$)	ΔR_z ($\mu g/cm^2$)	Φ (^{4}He) (10^{17} atom/cm^2)	C_0 (peak) (at.%)
$^{197}_{79}$Au	(fcc)	19.3	2.52	36	15	7.8	187	443	3.3	24
$_{73}$Ta	(bcc)	16.6	2.67	42	15	8.1	157	236	6.7	83
$^{27}_{13}$Al	(fcc)	2.70	6.78	38	10	6.7	54	59	3.9	26
$_{12}$Mg	(hex)	1.74	7.30	40	15	5.2	57	55	5.4	44
$^4_2$He	(hex)	0.12[d]	12.9	...	...	...	...	...	...	...

[a] Specified as face centered cubic, body centered cubic, or hexagonal.
[b] For the pure host metal at $E(^{18}\text{O}) = 19.7$ MeV. From Ref. 16.
[c] The specific energy loss for 36–42 keV ^{4}He ions in the NaCl protective layer is ~0.6 keV $cm^2/\mu g$. The ^{4}He energies incident on the metals are therefore less than $E(^4\text{He})$ by 6–9 keV.
[d] Liquid ^{4}He.

nance energy E_r' from E_r thus provides a direct measure of the mean depth of the ^{4}He distribution in the host metal. The true resonance width Γ_r can then be easily unfolded from the apparent resonance width Γ_r' to yield the width of the ^{4}He distribution $\Gamma(^4\text{He})$. These values of $(E_r' - E_r)$ and $\Gamma(^4\text{He})$, given in energy units, were then converted to the corresponding range and distribution parameters R_z and ΔR_z, using the indicated values of $dE/d(\rho x)[^{18}\text{O}]$, as given in Table V. Note that R_z specifies the mean *projected* range, and ΔR_z is defined to be the full width at half-maximum (FWHM) of the distribution of ranges.

The integrated absolute yield of the experimental resonance curves provides a direct measure of the total implanted areal density of ^{4}He (defined as Φ) and also the concentration C_0 corresponding to the peak of the ^{4}He distribution. Here C_0 denotes the percentage of ^{4}He atoms expressed as a fraction of the original (100%) host atoms.

The experimental data of Fig. 9 indicate clearly the optimum ^{18}O bombarding energy for resonant production of the ^{21}Ne $J^\pi = \frac{1}{2}^-$ level. The optimum energy for production of the $J^\pi = \frac{1}{2}^+$ state was calculated from these experimental data on R_z and ΔR_z, using the observed displacements of the resonance structure as observed by Switkowski *et al.*[33] Note that the resonance structure for production of the ^{21}Ne $J^\pi = \frac{1}{2}^+$ state is well fitted as a doublet, for the parameters given in Fig. 9.

As given in the main text (Sec. III B) the mean energy and effective width are $\langle E_r \rangle = 19.825$ MeV and $\langle \Gamma_r \rangle = 560$ keV. The ^{18}O bombarding energy which leads to maximum production of the $J^\pi = \frac{1}{2}^+$ state is then calculable from Table V as $E_B(^{18}\text{O}) = \langle E_r \rangle + \Delta E$, where $\Delta E \equiv R_z[dE/d(\rho x)]$ is the energy loss of the ^{18}O beam in arriving at the peak of the ^{4}He distribution. The bombarding energies (in MeV) calculated in this way are Au (20.30), Ta (20.24), Al (20.19), and Mg (20.24). The implantation energies $E(^4\text{He})$ were initially chosen to allow the same ^{18}O bombarding energy for all four targets. The observed differences indicate uncertainties due to such problems as surface contaminations, changes during implantation, uncertainties in the predicted R_z for both ^{4}He and ^{18}O, etc., and illustrate the desirability of measuring excitation functions, as we have done.

While the energies calculated above provide for maximum yield, it was felt to be more important to require that the mean reaction energy $\langle E(^{18}\text{O}) \rangle$ for production of the ^{21}Ne $J^\pi = \frac{1}{2}^+$ state be the same for all targets: because the mean γ-ray Doppler shift is proportional to $\langle E(^{18}\text{O}) \rangle^{1/2}$ this procedure reduces the possibility for systematic errors in the interpretation of the data. We choose $\langle E(^{18}\text{O}) \rangle = \langle E_r \rangle$, and the ^{18}O bombarding energies were de-

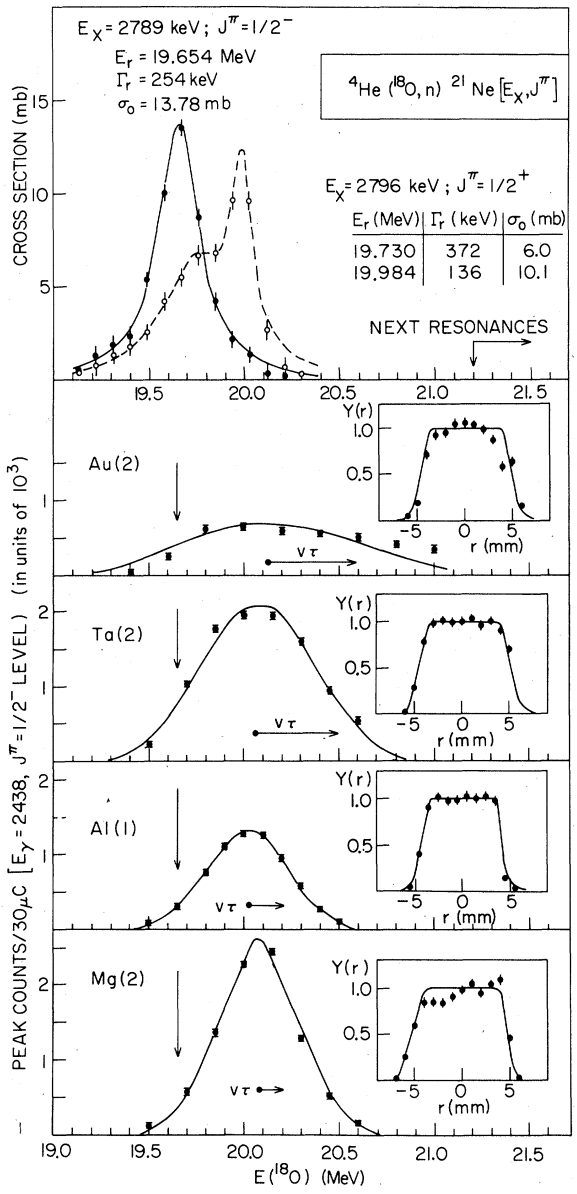

FIG. 9. Resonance cross sections (upper plot) for production of the ^{21}Ne $J^{\pi}=\frac{1}{2}^{+}$ and $\frac{1}{2}^{-}$ states via the ^{4}He(^{18}O,n)^{21}Ne* reaction: from the data on the inverse reaction as given in Ref. 33. The data are fitted with Breit-Wigner shapes for the resonance parameters indicated. The lower plots show γ-ray yield curves measured for production of the $J^{\pi}=\frac{1}{2}^{-}$ state via ^{18}O bombardment of ^{4}He-implanted targets. These data were fitted with Gaussian shapes, as shown, to determine the distribution of ^{4}He in the implanted target, as characterized by the data on R_z, ΔR_z, Φ, and C_0 given in Table V. For comparison the mean recoil decay distance $v\tau$ is shown for $v/c=0.04$ and $\tau=8$ fs. For each target, the inset shows a scan of the circular target spot along a diameter, illustrating the relative uniformity of the implantation.

termined by folding in the actual $J^{\pi}=\frac{1}{2}^{+}$ resonance structure with the observed ^{4}He distributions. These energies (in MeV) for the four targets are Au (20.60), Ta (20.30), Al (20.25), and Mg (20.30). These latter values are uniformly greater than the first set because of the interplay between the widths of the doublet resonance structure and the variation of ^{4}He distribution widths for the four different targets (see Fig. 9 and Table V).

In Table VI the experimental distribution parameters R_z and ΔR_z are compared to the values taken from the compilation of Zeigler,[57] given as R_z' and $\Delta R_z'$. The values of R_z' correspond to the ^{4}He energies actually incident on the metal, i.e., after correcting for the energy loss in the NaCl layer (see Table V). Values of $\Delta R_z'$ correspond to the incident energies, $E(^{4}\mathrm{He})$ of Table V, because of the expectation that the net straggling in ranges is proportional to the total ^{4}He energy loss.

The predicted values for $\Delta R_z'$ are seen to be somewhat less than the experimental values ΔR_z by 20–30%. Noting an exception for the Al target, the predicted R_z' are ~10% larger than the experimental R_z, in a direction that could be explained by a small buildup of carbon during the implantation. The reflection coefficients $\mathcal{R}$, computed from Refs. 58 and 59, are also shown in Table VI; surface corrections have been applied. The expected areal density of ^{4}He is then computed from the Φ_{inc} of Table V as $\Phi'=(1-\mathcal{R})\Phi_{\mathrm{inc}}$.

Comparison of Φ' and Φ, as given in Table VI, indicates that for both the Au and Al targets only 50–60% of the ^{4}He was actually retained in the metal, while for Ta and Mg the retention is ~100%.

In the following subsections we wish to estimate the effect which the ^{4}He implantations have on the specific energy loss for ^{21}Ne ions within the implanted regions. In order to allow for the possibility that the effect may be intermediate between the concentrations corresponding to Φ' and Φ, we adopt for this purpose the intermediate values C_0 given in Table VI, where the quoted errors on C_0 have been set large enough to encompass areal implantation densities ranging from Φ' to Φ.

Similar measurements for the first set of targets showed reasonably good agreement between observed and predicted ^{4}He distributions. However, the Mg target implanted to a dose of 6.7×10^{17} ^{4}He-atoms/cm^{2} exhibited a discoloration over ~20% of the central area: The radial scan of the yield indicated little ^{4}He in this area, and only the peripheral region was used in the DSA measurements. In view of this observation, the Mg target for the second set was implanted to a lesser areal density, as indicated in Table V, and no such problems were encountered. The range R_z for the Al target was markedly less than the prediction from

TABLE VI. Comparison of the implanted ^{4}He profiles predicted by transport theory to those deduced from experiment. R_z and ΔR_z are the mean range and FWHM of the range distribution and Φ is the areal density of the implanted ^{4}He. The predicted ranges are from Ref. 54, while the reflection coefficients $\mathcal{R}$ are from Refs. 55–57. For comparison, the mean ^{21}Ne recoil decay distance is $v\tau = 0.096$ μm, for $v/c = 0.04$ and $\tau = 8$ fs. The values adopted for the peak concentration C_0 are indicated.

	Predicted				Experiment			
Host metal	R_z' (μm)	$\Delta R_z'$ (μm)	$\mathcal{R} \equiv$ reflection coeff.	Φ' [a] (10^{17} atom/cm^2)	R_z (μm)	ΔR_z (μm)	Φ (10^{17} atom/cm^2)	C_0 adopted (at. %)
Au	0.097	0.155	0.15	6.6	0.097	0.230	3.3	32 ± 8
Ta	0.107	0.126	0.13	7.0	0.094	0.141	6.7	83 ± 10
Al	0.314	0.178	0.01	6.6	0.200	0.219	3.9	32 ± 8
Mg	0.385	0.207	0.01	5.2	0.328	0.316	5.4	44 ± 8

[a] Computed from the Φ_{inc} of Table V as $\Phi' = (1 - \mathcal{R})\Phi_{inc}$.

Zeigler,[57] which may result from an erosion of the surface metal due to the implantation. The second Al target was therefore implanted at a lower ^{4}He beam current (20 μA) for a dose of only 4.7×10^{17} atoms/cm^2. Although the mean range R_z agreed more closely with prediction, the retained ^{4}He was again only ~50% of the bombardment dose. Accordingly, the second set of DSA measurements employed the Al target made in the first production run, because the yield was a factor of ~2 greater.

3. Effect of the implantation on dv/dt

The stopping power $dE/d(\rho x)$ for the implanted areas may be calculated for the atomic concentrations given in Table VI using Bragg's law and tabulated stopping powers for the host material and implanted ^{4}He. However, the quantity that is required for interpretation of the DSA data is the slowing power dv/dt (or alternatively dE/dx) which can be obtained only if we can establish the appropriate density for the implanted region. It is therefore necessary to consider quantitatively the extent to which the implanted ^{4}He may have deformed (expanded) the lattice structure of the host medium, and perhaps also the form in which it is retained.

There are two main bodies of evidence which may be brought to bear on this question: (i) a quasitheoretical interpretation based on our understanding of the implantation mechanism, and (ii) empirical evidence on stopping powers derived from previous implantation experiments. The conclusion from these two considerations, discussed separately in the following subsections, is that the stopping power in the implanted region is less than that of the pure host material, in an amount approximately equal to that provided by the expansion due to the implanted He atoms.

The importance of the latter conclusion can be better understood from a simple calculation of the relative volumes of the implanted He and that of the target layer in which it is imbedded. At liquid density (0.12 g/cm^3), a dosage of 6.7×10^{17} He atoms/cm^2 corresponds to a layer 0.38 μm thick: this should be contrasted to the implantation thicknesses ΔR_z (0.1–0.3 μm) in which the ^{4}He occupies only a fraction of the total volume.

4. Slowing power: theoretical

It is well known that the solubility of noble gasses in metals is very low—corresponding to only a few parts per million (ppm). At concentrations of 100–200 ppm for ^{3}He implanted in W, Picraux and Vook[60] demonstrated via channelling investigations that the ^{3}He was located substitutionally in clusters of 2 and 3 helium atoms per substitutional site, with clusters of 3 appearing more frequently than clusters of 2. The possibility of clusters involving >3 helium atoms was explored in theoretical calculations by Wilson, Baskes, and Bisson.[61] For He implanted in an fcc metal (specifically Cu) they found that complexes of 5–8 He atoms in a vacancy could form rapidly at room temperature. The most probable cluster was 6-He atoms per vacancy (He_6V), and clusters involving fewer He atoms would rapidly coalesce into the He_6V configuration. The volume change associated with such clusters, as calculated by Baskes and Holbrook,[62] corresponds to pressures in the range ~1.5×10^6 atm for the He_6V configuration.

As the implanted concentrations are raised into the region of a few percent, He bubbles 15–30 Å diameter are apparent under examination with electron microscopy.[63] However, these bubbles, which are several hundred Å apart and correspond to a volume density of ~10^{15} bubbles/cm^3, contain only a percent or so of the total stored He. Final-

ly, at concentrations greater than 100% (corresponding to doses $>10^{18}$ He-atoms/cm^2) the bubbles are observed to coalesce into very large (>300 Å) bubbles which eventually rupture through the surface. Investigations of such destructive processes (blistering, exfoliation) suggest a critical saturation whose value is inversely proportional to temperature.[64] For the cases studied here it would appear that, for $T<200$ °C, this critical concentration would be $\gtrsim 5\times10^{18}$ atoms/cm^2, i.e., ~7 times greater than that employed for the He-implanted targets.

In the region below this critical concentration, the considerations surveyed suggest that the most likely mechanism for the storage of large amounts of ^{4}He involves substitutional clusters of He_nV, with $n\simeq 6$ the dominant configuration. Some fraction of the ^{4}He would undoubtedly be stored interstitially, but the probability for finding individual ^{4}He atoms at substitutional sites should be low, following the expectation that such configurations would be rapidly superseded by configurations of $n>1$.

In the following we examine the volume changes expected for both substitutional and interstitial configurations. Because the theoretical calculations do not include all of the specific cases considered, nor all ranges of concentrations, we quote central values with assigned errors encompassing the range of the calculational variation. As will be seen, this has only a slight effect on the final conclusions.

Interstitial Placement. Calculations for the volume expansion due to interstitial placement of He atoms in bcc metals has been given by Johnson, Bisson, and Wilson[65] in terms of the unit volume Ω of the host atoms, from which we adopt a central value $\Delta V=(0.65\pm0.25)\Omega$. The net fractional volume expansion for a concentration C_0 is thus

$$\Delta V/V=C_0(0.65\pm0.25),$$

where again C_0 is the peak ^{4}He concentration.

Substitutional Placement. If the ^{4}He is stored in substitutional sites in the form He_nV, one then has (C_0/n) such clusters and correspondingly (C_0/n) host atoms displaced into interstitial locations. We take $(0.75\pm0.25)\Omega$ as an estimate of the expansion due to interstitial host displacements. For the He_nV clusters we use the results of Baskes and Holbrook,[62] who conclude that the volume expansion for individual clusters is nearly linear in n, being given (for ^{4}He in Cu) by $\Delta V=(-0.80+0.60n)\Omega$. The net fractional volume expansion corresponding to an atomic concentration C_0, computed as the sum of these terms, is

$$\Delta V/V=C_0(0.60-0.05/n).$$

As can be seen, the result is only slightly sensitive to n.

The interesting conclusion from this exercise is that the implantation brings about a net volume expansion whose magnitude is nearly independent of the mode of storage. For the following discussion we therefore adopt the average of the above results,

$$\Delta V/V=C_0(0.6\pm0.2),$$

in order to compute the effect of the implantation on the specific energy loss parameters.

The results of this computation are shown in Table VII. The fractional volume changes $\Delta V/V$ are specifically for the listed peak concentrations C_0. Within this expanded volume, the presence of the implanted ^{4}He brings about a change $\Delta m/m$ in the net mass and a change in the slowing power defined as $\Delta s/s$. The resultant fractional change $\Delta\epsilon/\epsilon$ in the total specific stopping power ($\epsilon\equiv dE/dx$), or alternatively in the total slowing power dv/dt, is obtained directly from $\Delta V/V$ and $\Delta s/s$, and does not involve $\Delta m/m$. [Conversely, $dE/d(\rho x)$ does depend on the latter term.]

The reductions in dv/dt specified by the quoted values of $\Delta\epsilon/\epsilon$ are appropriate only for the peak concentrations C_0. Recoiling ^{21}Ne will of course travel through a range of target material, and thus the average C_0 and $\langle\Delta\epsilon/\epsilon\rangle$ will be somewhat reduced for practical cases. In the last column of Table VII we show the reduced values of $\langle\Delta\epsilon/\epsilon\rangle$ calculated for an 8-fs mean life for the experimental conditions employed in the measurement of the ^{21}Ne 2796-keV lifetime. These values were used in conjunction with the dE/dx for the pure host materials (Tables VII and II) in analyzing the DSA data.

5. Slowing power: experimental

Of the many experiments carried out using implanted targets, almost none provide any direct evidence on the change in slowing power dv/dt due to the implantation. In several early experiments targets implanted to saturation were employed to measure resonance widths (Γ) or resonance integrals $[\int\sigma(E)dE]$ with considerable precision. However, the parameter of interest in these cases is $dE/d(\rho x)$, and therefore the effect of a volume expansion would not influence the interpretation of the results or the conclusions. Conversely, earlier DSA measurements involved lifetimes sufficiently long (relative to the slowing down time) that the effects of the implantation would appear only as minor perturbations in the measurement. The expected effects were subsequently allowed

TABLE VII. Summary of changes in specific stopping powers ($\epsilon \equiv dE/dx$) due to implantation of ^{4}He at the indicated atomic concentrations C_0. Here $\Delta V/V$ defines the volume expansion, while $\Delta m/m$ and $\Delta s/s$ account for the added mass and slowing down (within this expanded volume) due to the presence of the ^{4}He atoms. The last two columns show the peak values and the mean values (appropriate for $\tau = 8$ fs) of the fractional change in ϵ. These data are specifically for ^{21}Ne ions of velocity $v/c = 0.04$ corresponding to $E(^{21}\text{Ne}) = 15.9$ MeV.

Host material	C_0 [a] (at.%)	ϵ (^{21}Ne) (MeV/μm)	$\frac{\Delta V}{V}$ (%)	$\frac{\Delta m}{m}$ (%)	$\frac{\Delta s}{s}$ (%)	$\Delta\epsilon/\epsilon$ (peak value)	$\langle\Delta\epsilon/\epsilon\rangle$ [b] (average value)
Au	32 ± 8	6.64	19	0.6	3.8	−0.16	−0.10 ± 0.04
Ta	83 ± 10	5.79	50	1.8	10.6	−0.44	−0.21 ± 0.08
Al	32 ± 8	2.51	19	4.7	10.2	−0.11	−0.07 ± 0.03
Mg	44 ± 8	1.77	26	7.2	14.3	−0.16	−0.11 ± 0.05
^{4}He	...	0.24	...	...	...	...	...

[a] For the second set of targets.

[b] The uncertainties are propagated from the quoted uncertainties in C_0 with a 30% uncertainty in $\Delta V/V$ added in quadrature.

for by increasing the quoted uncertainty on the measured values for the lifetime.

Recently, Bister, Anttila, and Keinonen[66] have reported DSA measurements in the ^{22}Ne$(p,\gamma)^{23}$Na reaction which were utilized to investigate the character of Ne-implanted targets. Ta blanks were implanted to a saturation dose of 6 μg/cm^2 of ^{22}Ne at 80-keV ion energy, and were used to measure the Doppler-shift attenuation of the ^{23}Na 2640-keV γ ray observed at the $E_p = 1005$-keV resonance. Measurements made at the peak of the resonance curve yielded the result $F(\tau) = (32.5 \pm 0.5)\%$, while at a somehwat higher bombarding energy (corresponding to the tail of the resonance yield where the ^{22}Ne concentration is markedly less) the results were $F(\tau) = (30.7 \pm 0.5)\%$. As noted by the authors, "this indicates higher stopping in that part of the Ta where there are less ^{22}Ne atoms than at the maximum concentration." For comparison, the values of τ computed under the assumption that the slowing power is that of pure Ta, are 103 ± 5 and 112 ± 5 fs, respectively.

These results of Blister, Anttila, and Keinonen[66] are thus both qualitatively and also quantitatively in accord with the conclusions reached in subsection 4 above. Note that for $\tau \sim 100$ fs, the ^{23}Na recoil velocity obtained in the (p,γ) reaction at $E_p \sim 1$ MeV is yet so low—$v/c \sim 0.0002$—that the product $v\tau \sim 0.07$ μm is again comparable to the spatial thickness of the ^{22}Ne-implanted region.

From a quite different viewpoint, Eernisse and Picraux[67] have made direct measurements of the volume expansions induced by the implantation of ^{4}He into thin metal plates of Mo, Nb, and Al. The experiment utilized a precision mechanical apparatus to observe the distortion of plates due to implantations in the range of ^{4}He fluences 10^{14}–10^{18} ions/cm^2, thus providing a direct measure of the volume expansion $\Delta V/V$. At low intensities ($<10^{15}$ ions/cm^2) the expansion appears linear with ^{4}He concentration, while at higher intensities the expansion is less rapid. These results would appear to be in at least semiquantitative agreement with the volume expansions deduced in subsection 4 above.

[1] B. H. J. McKellar, Contribution to the Third Vacation School of the Australian Institute of Physics, Jindabyne, New South Wales, 1977 (unpublished); R. A. Brandenburg, B. H. J. McKellar, and I. Morrison, Phys. Rev. Lett. 41, 618 (1978).

[2] E. G. Adelberger, in Proceedings of the Ben Lee Memorial International Conference on Parity Non-conservation, Weak Neutral Currents and Gauge Theories, 1977, Fermi National Acclerator Laboratory (unpublished).

[3] K. A. Snover, R. von Lintig, E. G. Adelberger, H. E. Swanson, T. A. Trainor, A. B. McDonald, E. D. Earle, and C. A. Barnes, Phys. Rev. Lett. 41, 145 (1978).

[4] D. J. Millener, E. K. Warburton, K. S. Snover, R. von Lintig, and P. G. Ikossi, Phys. Rev. C 18, 1878 (1978).

[5] P. M. Endt and C. Van der Leun, Nucl. Phys. A310, 1 (1978).

[6] H. Grawe, F. Heidinger, and K. Kändler, Z. Phys. A280, 271 (1977).

[7] A mean life of 10 ± 4 fs was reported for the 2796-keV level in Ref. 6. However, for the reasons discussed in Sec. IV, we interpret this result as an upper limit $\tau < 20$ fs.

[8] R. D. Bent, J. E. Evans, G. C. Morrison, N. H. Gale,

and I. J. van Heerden, Nucl. Phys. A90, 122 (1967).
[9]C. Rolfs, E. Kuhlmann, F. Riess, and R. Kraemer, Nucl. Phys. A167, 449 (1971).
[10]J. G. Pronko, C. Rolfs, and H. J. Maier, Nucl. Phys. A111, 561 (1967); Phys. Rev. 186, 1176 (1969).
[11]D. C. Bailey, P. E. Carr, J. L. Durell, A. N. James, M. W. Greene, and J. F. Sharpey-Schafer, J. Phys. A 4, 908 (1971).
[12]D. B. Fossan and E. K. Warburton, in *Nuclear Spectroscopy and Reactions, Part C*, edited by J. Cerny (Academic, New York, 1974), p. 307.
[13]E. K. Warburton, J. W. Olness, G. A. P. Engelbertink, and T. K. Alexander, Phys. Rev. C 7, 1120 (1973).
[14]J. S. Forster, D. Ward, G. J. Costa, G. C. Ball, W. G. Davies, and I. V. Mitchell, Phys. Lett. 51B, 133 (1974); J. S. Forster, G. C. Ball, C. Broude, W. G. Davies, and I. V. Mitchell, Phys. Rev. C 14, 596 (1976).
[15]D. I. Porat and K. Ramavataram, Proc. Phys. Soc. (London) 78, 1135 (1961).
[16]L. C. Northcliffe and R. F. Schilling, Nucl. Data A7, 233 (1970).
[17]L. C. Northcliffe, Phys. Rev. 120, 1744 (1960).
[18]D. Ward, J. S. Forster, H. R. Andrews, I. V. Mitchell, G. C. Ball, W. G. Davies, and G. J. Costa, AECL-5313, 1976 (unpublished).
[19]J. F. Ziegler and W. K. Chu, At. Data Nucl. Data Tables 13, 463 (1974).
[20]J. S. Forster, D. Ward, H. R. Andrews, G. C. Ball, G. J. Costa, W. G. Davies, and I. V. Mitchell, Nucl. Instrum. Methods 136, 349 (1976).
[21]D. Schwalm, E. K. Warburton, and J. W. Olness, Nucl. Phys. A293, 425 (1977).
[22]K. Braune, Staatsexamensarbeit 1977, Heidelberg (unpublished).
[23]E. K. Warburton, D. E. Alburger, and D. H. Wilkinson, Phys. Rev. 129, 2180 (1963).
[24]E. K. Warburton, J. W. Olness, and A. R. Poletti, Phys. Rev. 160, 938 (1967).
[25]This parametrization has also been utilized by the Utrecht group, see e.g., Ref. 31.
[26]N. Bohr, K. Dan. Vidensk. Selsk. Mat. Fys. Medd. 18, No. 8 (1948); see Eq. (20a) of Ref. 21.
[27]D. Branford and I. F. Wright, Nucl. Instrum Methods 106, 437 (1973); I. F. Wright, B. E. Cooke, L. K. Fifield, and A. R. Poletti, in Proceedings of the International Conference on Nuclear Interactions, Canberra, Australia, 1978 (to be published).
[28]T. D. Newton, Phys. Rev. 78, 490 (1950).
[29]J. S. Forster, T. K. Alexander, G. C. Ball, W. G. Davies, I. V. Mitchell, and K. B. Winterbon, Nucl. Phys. A313, 397 (1979).
[30]L. K. Fifield, J. Asher, and A. R. Poletti, J. Phys. G 4, L65 (1978).
[31]L. P. Ekström, D. E. C. Scherpenzeel, G. A. P. Engelbertink, H. J. M. Aarts, and H. H. Eggenhuisen, Nucl. Phys. A295, 525 (1978).
[32]T. K. Alexander, G. C. Ball, W. G. Davies, and J. S. Forster, Nucl. Phys. A313, 425 (1979).
[33]Z. E. Switkowski, S. R. Kennelt, D. G. Sargood, B. M. Spicer, and R. O'Brien, Phys. Rev. C 16, 1264 (1977).
[34]J. L. Black and W. Gruhle, Nucl. Instrum. Methods 46, 213 (1967).
[35]R. C. Greenwood, R. G. Helmer, and R. J. Gehrke, Nucl. Instrum. Methods 159, 465 (1979).
[36]R. C. Greenwood and R. E. Chrien, in Proceedings of the Third International Symposium on Neutron Capture γ-ray Spectroscopy and Related Topics, 1978, Brookhaven National Laboratory (unpublished).
[37]In obtaining this average an uncertainty in $dE/d(\rho x)$ of 4% in all four targets was treated as a common systematic error. Considering the common extrapolation procedure (see Sec. II) used to obtain the various values of $dE/d(\rho x)$, the practice in some previous DSA analysis of treating the uncertainties in $dE/d(\rho x)$ as independent (see, e.g., Ref. 31) is certainly incorrect.
[38]J. A. J. Hermans, G. A. P. Engelbertink, M. A. van Driel, H. H. Eggenhuisen, and D. Bucurescu, Nucl. Phys. A255, 221 (1975).
[39]M. Bister and A. Anttila, Nucl. Instrum. Methods 77, 315 (1970). See Ref. 40 for a recent application and list of recent references.
[40]M. Bister, A. Anttila, and J. Keinonen, Phys. Rev. C 16, 1303 (1977).
[41]D. S. Andreev, A. F. Afonin, V. K. Boudarev, A. P. Grinberg, K. I. Erokhina, and I. Kh. Lemberg, Izv. Akad. Nauk. (Ser. Fiz.) 32, 1671 (1968).
[42]A. E. Blaugrund, Nucl. Phys. 88, 501 (1966).
[43]The original analysis of Pronko, Rolfs, and Maier (Ref. 10) used the treatment due to this laboratory (Refs. 23,24) and Sec. II; however, their analysis contains several numerical errors and an inadequate representation of the nuclear stopping and scattering. Using the present prescription for the nuclear stopping parameter K_n (Sec. II) we find better agreement with the Blaugrund treatment. For instance, $\tau = 110$ fs for the 1747-MeV level versus 150 fs from Pronko, Rolfs, and Maier. Nevertheless, the treatment of Sec. II, is not suited to the low velocity DSA where nuclear scattering is important. In this region of velocity the Blaugrund treatment is clearly superior although it too contains computational uncertainties, estimated to be $\lesssim 10\%$.
[44]Actually our analysis gives results of 76 ± 20 and 65 ± 18 fs for the 1.75- and 2.87-MeV levels, respectively. Bailey *et al.* (Ref. 11) also re-analyzed the DSA results of Pronko, Rolfs, and Maier (Ref. 10) via the Blaugrund method and obtained 65 ± 20 and 50 ± 15 fs, respectively, $\sim 12\%$ lower than Table III. Note that the uncertainties do not include the discussed contributions from $dE/d(\rho x)$, ρ, and the analysis. The spread in results suggests the possibility of real differences between the various computer programs based on the Blaugrund treatment.
[45]D. J. Millener (unpublished), see Sec. IV B of Ref. 4 for a description of this calculation. We wish to thank Dr. Millener for providing us with these results.
[46]T. T. S. Kuo and G. E. Brown, Nucl. Phys. 85, 40 (1966).
[47]W. Chung, Ph.D. thesis, Michigan State University, 1976 (unpublished); see also Ref. 21.
[48]S. J. Skorka, J. Hertel, and T. W. Retz-Schmidt, Nucl. Data A2, 347 (1966).
[49]See Table II of Ref. 4.
[50]See Table I of Ref. 4 for a SU3 decomposition of the $\frac{3}{2}^+$, $\frac{5}{2}^+$, and $\frac{1}{2}^+$ wave functions.
[51]E. Selin, S. E. Arnell, and O. Almén, Nucl. Instrum. Methods 56, 218 (1967).

[52]A. Anttila, M. Bister, A. Fontell, and K. B. Winterbon, Radiat. Eff. 33, 13 (1977).
[53]J. Keinonen, M. Riihonen, and A. Anttila, Phys. Rev. C 15, 579 (1977).
[54]B. M. U. Scherzer, H. L. Bay, R. Behrisch, P. Børgesen, and J. Roth, Nucl. Instrum. Methods 157, 75 (1978).
[55]W. Möller, M. Hufschmidt, and D. Kamke, Nucl. Instrum. Methods 140, 157 (1977).
[56]This technique was suggested in the work of Ekström *et al.*, Ref. 31.
[57]*The Stopping and Ranges of Ions in Matter*, organized by J. F. Ziegler (Pergamon, New York, 1977), Vol. 4.
[58]J. Bøttinger, J. A. Davies, P. Sigmund, and K. B. Winterbon, Radiat. Eff. 11, 69 (1971).
[59]K. B. Winterbon, *Ion Implantation Range and Energy Deposition Distributions* (Plenum, New York, 1975), Vol. 2.
[60]S. T. Picraux and F. L. Vook, in Proceedings of the International Conference on *Applications of Ion Beams to Metals*, 1973, Albuquerque, edited by S. T. Picraux, E. P. Eernisse, and F. L. Vook (Plenum, New York, 1974), p. 407.
[61]W. D. Wilson, M. I. Baskes, and C. L. Bisson, Phys. Rev. B 13, 2470 (1976).
[62]M. I. Baskes and J. H. Holbrook, Phys. Rev. C 17, 422 (1978).
[63]A. N. Goland, in *Atomic Structure and Mechanical Properties of Metals*, Proceedings of the International School of Physics "Enrico Fermi," Course LXI, Varenna, 1974, edited by G. Caglioti (North-Holland, Amsterdam, 1976). These lectures provide an excellent review of the topics of general interest to the present considerations.
[64]G. J. Thomas and W. Bauer, see Ref. 60, p. 533.
[65]R. A. Johnson, C. L. Bisson, and W. D. Wilson, Radiat. Eff. 25, 155 (1975).
[66]M. Bister, A. Anttila, and J. Keinonen, Nucl. Phys. A306, 189 (1978).
[67]E. P. Eernisse and S. T. Picraux, J. Appl. Phys. 48, 9 (1977).